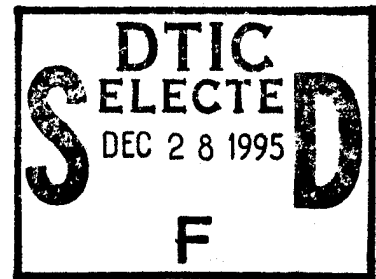


DYNAMIC IMPACT RESPONSE BEHAVIOR  
OF POLYMERIC MATERIALS (II)



FINAL REPORT  
(26 August 1977 to 26 October 1978)

March 1979

no AD #  
as of  
12/3/88

19951215 089

Prepared Under Contract N00019-77-C-0441

For  
Naval Air Systems Command  
Department of the Navy  
Washington, DC 20361

By  
Corporate Research and Development  
General Electric Company  
Schenectady, NY 12301

APPROVED FOR PUBLIC RELEASE; DISTRIBUTION UNLIMITED

DEPARTMENT OF DEFENSE  
PLASTICS TECHNICAL EVALUATION CENTER  
ARRADCOM, DOVER, N. J. 07801

SRD-79-056

DTIC QUALITY INSPECTED 1

PLASTICS  
TECHNICAL  
EVALUATION  
CENTER  
ARRADCOM  
DOVER, N. J.  
07801

DYNAMIC IMPACT RESPONSE BEHAVIOR  
OF POLYMERIC MATERIALS (II)

FINAL REPORT  
(26 August 1977 to 26 October 1978)

March 1979

Accesion For	
NTIS	CRA&I
DTIC	TAB
Unannounced	
Justification _____	
By _____	
Distribution / _____	
Availability Codes	
Dist	Avail and/or Special
A-1	

Prepared Under Contract N00019-77-C-0441

For

Naval Air Systems Command  
Department of the Navy  
Washington, DC 20361

By

Corporate Research and Development  
General Electric Company  
Schenectady, NY 12301

APPROVED FOR PUBLIC RELEASE; DISTRIBUTION UNLIMITED

Unclassified

B032735  
A045121

SECURITY CLASSIFICATION OF THIS PAGE (When Data Entered)

REPORT DOCUMENTATION PAGE		READ INSTRUCTIONS BEFORE COMPLETING FORM
1. REPORT NUMBER	2. GOVT ACCESSION NO.	3. RECIPIENT'S CATALOG NUMBER
4. TITLE (and Subtitle)  Dynamic Impact Response Behavior of Polymeric Materials (II)		5. TYPE OF REPORT & PERIOD COVERED  Final Report 26 Aug 77 to 26 Oct 78
7. AUTHOR(s)  William B. Hillig		6. PERFORMING ORG. REPORT NUMBER SRD-79-056
9. PERFORMING ORGANIZATION NAME AND ADDRESS  General Electric Company Corporate Research and Development P.O. Box 8, Schenectady, NY 12301		10. PROGRAM ELEMENT, PROJECT, TASK AREA & WORK UNIT NUMBERS
11. CONTROLLING OFFICE NAME AND ADDRESS  U.S. Naval Air Systems Command Washington, DC 20361		12. REPORT DATE March 1979
14. MONITORING AGENCY NAME & ADDRESS (if different from Controlling Office)		13. NUMBER OF PAGES 69
15. SECURITY CLASS. (of this report)  Unclassified		
15a. DECLASSIFICATION/DOWNGRADING SCHEDULE		
16. DISTRIBUTION STATEMENT (of this Report)  APPROVED FOR PUBLIC RELEASE: DISTRIBUTION UNLIMITED		
17. DISTRIBUTION STATEMENT (of the abstract entered in Block 20, if different from Report)		
18. SUPPLEMENTARY NOTES		
19. KEY WORDS (Continue on reverse side if necessary and identify by block number)  Hopkinson Bar Ballistic Impact Impact Damage of Polymers		
20. ABSTRACT (Continue on reverse side if necessary and identify by block number)  This report describes the work performed in the 14-month period beginning August 26, 1977, relating to a basic study of the materials response processes primarily of polymethylmethacrylate PMMA, polycarbonate PC, and epoxy resins during a ballistic impact encounter. Experimental impact data on PMMA, PC, and epoxy have been obtained using 19 and 4.5 mm diameter strikers at impact velocities of 1.77 and 2.93 m/sec. The data have been analyzed. The irreversible work absorbed by the specimen for a given impact energy, the depth of		

Unclassified

SECURITY CLASSIFICATION OF THIS PAGE(When Data Entered)

penetration, and the pulse duration increase in the order PMMA < epoxy < PC, but the irreversible energy per unit penetration is the reverse of this series. The apparent crater depth at the time of projectile/specimen separation shows less regular relative behavior. Cinematographic documentation of the impact process was made of PC and PMMA impacted by a 4.5 mm steel ball at an impact velocity of 120 m/sec. The camera speed was  $2 \times 10^5$  frames/sec. Densification could be clearly observed developing in the case of PC, and less distinctly so in the case of PMMA. Evidence for crack formation during the projectile rebound phase was noted for the case of PMMA. Some shrinkage of the densified zone appeared to occur subsequent to the impact. In another experiment, an impact pulse was obtained on a PMMA specimen struck by a 4.5 mm steel ball at 85 m/sec. This result indicates that attention must be given to eliminating or correcting the taper-on effect at the leading edge of the sensed pulse.

Unclassified

SECURITY CLASSIFICATION OF THIS PAGE(When Data Entered)

## TABLE OF CONTENTS

	Page
SUMMARY	v
1. INTRODUCTION	1-1
1.1 Recent Studies	1-3
1.2 Present Objectives	1-5
2. MATERIALS AND SPECIMEN PREPARATION	2-1
2.1 Polymethylmethacrylate	2-1
2.2 Polycarbonate	2-1
2.3 Epoxy	2-1
2.4 Inorganic Glass	2-1
3. IMPACT BAR STUDIES	3-1
3.1 PMMA Bar	3-1
3.1.1 Changes in Propagated Pulse Shape	3-1
3.1.2 Dispersion Observations	3-6
3.2 Aluminum Impact Bar	3-10
3.2.1 Description of the Aluminum Bar Apparatus and Alignment Procedures	3-10
3.2.2 Critical Testing of the Bar Apparatus	3-12
3.3 Impact Measurement Results	3-16
3.4 Commentary on Pendulum Impact Results	3-18
3.5 Ballistic Impact Using Air Gun	3-19
4. HIGH SPEED CINEMATOGRAPHY OF THE IMPACT PROCESS	4-1
4.1 The Experimental Arrangement	4-2
4.2 Experimental Results	4-4
5. DISCUSSION	5-1
6. ACKNOWLEDGMENT	6-1
7. REFERENCES	7-1
FIGURES	following page 7-1
APPENDIX	

## SUMMARY

This report describes the work performed in the 14-month period beginning August 26, 1977, relating to a basic study of the materials response processes primarily of polymethylmethacrylate PMMA, polycarbonate PC, and epoxy resins during a ballistic impact encounter. The work has included the sensing and recording of the impact stress pulses, using an instrumented Hopkinson impact bar, of sufficient quality to permit a detailed calculation of the material response. In addition, direct observations of representative impact events have been recorded using very high speed cinematography.

The objective of the present work was to refine the apparatus as needed and to obtain basic property and materials response data at increasingly high contact velocities. This is part of a longer range goal encompassing this, past, and anticipated future work of developing a scientific understanding of impact to develop a reliable data base. It is hoped that this can lead to better materials, better means of characterization, and a basis for theoretical modeling.

The experimental measurements consist of mounting a specimen of interest onto the end of a suitable impact bar and hitting the specimen with a striker carefully characterized with respect to mass, velocity, geometry, and position. This produces a stress pulse in the bar which is sensed by a strain gage, amplified, recorded in a digital storage oscilloscope, and finally computer analyzed to reveal the force, penetration depth, instantaneous velocity, energy transfer, and energy concentrated in the specimen. The original impact bar made of PMMA was found to exhibit substantial changes in pulse shape depending on the distance from the impact at which the pulse was sensed. This has been interpreted in terms of acoustic dispersion, partly due to intrinsic

material behavior and partly due to geometric factors. To minimize this problem, an aluminum bar has been substituted for the PMMA one. Calibration/validation experiments were run using glass and hot-pressed silicon carbide targets. These impacts can be accurately modeled theoretically. The results show excellent agreement with theory, except for a slight "tapering-on" effect in the leading edge portion of the pulse. This is believed due to dispersion even in the aluminum bar. Possible ways to correct for this are discussed.

Experimental impact data on PMMA, PC, and epoxy have been obtained using 19 and 4.5 mm diameter strikers at impact velocities of 1.77 and 2.93 m/sec. The data have been analyzed. The irreversible work absorbed by the specimen for a given impact energy, the depth of penetration, and the pulse duration increase in the order PMMA < epoxy < PC, but the irreversible energy per unit penetration is the reverse of this series. The apparent crater depth at the time of projectile/specimen separation shows less regular relative behavior.

Cinematographic documentation of the impact process was made of PC and PMMA impacted by a 4.5 mm steel ball at an impact velocity of 120 m/sec. The camera speed was  $2 \times 10^5$  frames/sec. Densification could be clearly observed developing in the case of PC, and less distinctly so in the case of PMMA. Evidence for crack formation during the projectile rebound phase was noted for the case of PMMA. Some shrinkage of the densified zone appeared to occur subsequent to the impact.

In anticipation of further work in which the impact bar will be used in conjunction with air gun fired projectiles, an impact pulse was obtained on a PMMA specimen struck by a 4.5 mm steel ball at 85 m/sec. These results indicate that further attention must be given to further eliminating or correcting for the taper-on effect at the leading edge of the sensed pulse.

## DYNAMIC IMPACT RESPONSE BEHAVIOR OF POLYMERIC MATERIALS (II)

### 1. INTRODUCTION

The present work is part of a continuing comprehensive study of indentation and impact phenomena particularly as they occur in two standard, relatively well-characterized, structural polymers, namely polymethylmethacrylate (PMMA) and polycarbonate (PC) resins. To a less extent, polymerized epoxy resin and inorganic glass have also been examined. The intent is to develop an understanding of the irreversible deformation, structural alteration, and mechanical failure mechanisms that occur when concentrated dynamic loads are applied to these materials. Among amorphous materials, PC has outstanding impact resistance. It is a continuing goal to determine the reason for these differences in behavior in sufficiently basic terms to allow analysis of the constituent phenomena in the expectation that this can contribute to a more precise characterization of impact resistance and to the evolution of more impact resistant polymeric materials.

Our approach has been to idealize the geometries sufficiently to facilitate theoretical modeling and, at the same time, to retain the essential features of typical impact encounters and concentrated loads experienced by these structural polymers under normal use. Therefore, a spherical striking body and an infinitely thick polymer were selected as the ideal configuration. Experimentally, 4.5 mm ball bearings and 12.5 mm thick polymer specimens have usually been used to approximate this ideal. In the experiments, a wide range of impact velocities and methods of loading have been used. In the work to date, impact velocities have spanned 9½ decades from  $8 \times 10^{-8}$  m/sec (.0002"/min) to almost

$3 \times 10^2$  m/sec ( $1000'$ /sec). The low velocities provide information in the more commonly studied regime in which the typical concern is the mechanical viscoelastic-plastic characterization of polymers. Increasing velocity allows study of the manner in which the expected increasing elastic behavior manifests itself, ultimately leading to brittle failure. The upper end of the velocity regime is of particular interest since it is at these velocities that the ballistic impacts of practical service experience occur. However, because measurements leading to data useful for basic analyses become increasingly difficult with increasing velocity, the practical upper limit appears to be about 300 m/sec.

Details of the prior work are given in the earlier reports.<sup>(1-5)</sup> Some of the important overall observations and conclusions to date are:

- 1) Standard linear viscoelastic models of polymer behavior have proven unreliable either as limiting laws at very low penetration rates or at small penetration depths, even at as little as 1% of the ball radius.
- 2) The penetration, and to a greater extent the rate of penetration, alters the structure of the polymer in such a way that the stress relaxation times are profoundly affected. The greater the rate of penetration, the smaller the characteristic delay time; thus, under a wide range of velocities, stress is able to decay away nearly as fast as it is applied.
- 3) Anelastic densification of the polymers occurs under the ball. The extent of densification is a function of the polymer and the depth of penetration, but it is relatively insensitive to velocity. This densification anneals out, and the permanent deformation resulting from impacts also anneals out when the polymer is heated to its glass transition temperature. Our work has shown that the recovery process does not involve viscous flow.

In earlier work<sup>(1-4)</sup> mechanical test machines of the types used for stressing metals and polymers could provide test velocities up to 2.5 m/sec. To make measurements at higher velocities, however, a new approach is necessary in which a spherically tipped mass or a ball is made to collide with the specimen. In this situation, an initial velocity can be selected, but the deceleration, duration of the impact, and all other dynamic variables are no longer independently adjustable. Furthermore, sensing the reaction force and the penetration can be done only indirectly by solving the equations of motion. This approach requires a precise knowledge of the reaction force as a function of time; however, the time scale is such that the rate of propagation of the stress through the specimen and the supporting structure become important considerations. This methodology was described in detail in the previous report.<sup>(5)</sup> Hence, only departures from this procedure will be discussed in the present report.

### 1.1 Recent Studies

Measurements were started during the preceding contractual study using an instrumented (Hopkinson) impact bar, in which the specimens were mounted on the end of a long PMMA bar 19 mm x 19 mm x 1.8 mm. The bar was supported at two places along its length by two bifilar strings in the general shape of a V. This allows the bar to swing freely along its axis, while substantially preventing sidewise displacement. A similar arrangement was used to support the striker. From the amplitude of the swing of the bar after the specimen is impacted by the striker and from the initial position of the striker before its release, the momenta and kinetic energies can be computed. Two striker geometries were used. One was a 19 mm, 28.3 g hard steel ball bearing. The other was a 42 g steel cylinder with one end in the form of a nose terminating in a 4.5 mm

diameter spherical cap. The latter geometry provided continuity with prior indentation work and with planned air gun work using 4.5 mm projectiles.

Strain gages on the bar connected to suitable bridge and amplifier circuits and finally to a digital storage oscilloscope allow the strain pulse produced by the impact to be recorded. Mathematical processing of the pulse data, using a simplified one-dimensional model for the stress distribution in the impact bar, allows the force, penetration depth, striker velocity, various energy terms, and momentum transfer to be computed, in principle. The reason for using the polymer PMMA as the impact bar was because this would minimize acoustic impedance mismatch problems in transmitting the impact pulse through the specimen block into the bar. Secondly, the small value of its Young's modulus resulted in a large strain for a given force. This was favorable with respect to signal-to-noise considerations.

However, PMMA is known to have an appreciable dependence of sound propagation velocity on frequency, so that change of the pulse shape as it travels down the bar was expected. In order to investigate this effect, inorganic glass is especially convenient, because its impact response can be accurately modeled using the Hertz theory. Hence, it served as a primary calibration medium. The experimental strain pulse obtained on glass had shapes that closely followed the theoretical pulse, except that onset (nose) of the measured pulse built-up in amplitude more gradually than predicted. However, the pulse duration, pulse half-width, and peak amplitude matched the theoretical shape well. The difference in the shape of the nose resulted in a computed force-penetration depth relationship that was in substantial variance with the known Hertz law relationship.

This suggested that acoustic dispersion was affecting the shape of the nose and that the pulse shape would require correction if the PMMA impact bar were to be capable of yielding the correct force law. Analysis of the pulse into Fourier frequency components was begun. This would allow each component to be separately translated according to its own characteristic velocity and then individual components resynthesized into a new dispersion corrected pulse shape. This analysis/synthesis work was only partially completed.

Impact pulse determinations were obtained on PMMA, PC, and epoxy in addition to glass. A semi-quantitative approach for analyzing the data was developed based on general pulse shape characteristics. This indicated that at an impact velocity of 2.5 m/sec, the 4.5 mm striker caused more irreversible damage than did the larger one, and that the level of damages decreased in the order PC, epoxy, PMMA, glass. However, such basic information as the force penetration dependence required the development of a satisfactory procedure to obtain a pulse shape free of distortion due to dispersion.

### 1.2 Present Objectives

The goals of the present effort were (1) to resolve the problems associated with the pulse shape, (2) to extend the range of measurements to higher impact velocities using the 4.5 mm diameter plus other projectile geometries, (3) to examine the impact process using high speed photographic techniques, and (4) to conduct theoretical and analytical studies of impact. Progress towards these goals is described in Sections 3 and 4.

## 2. MATERIALS AND SPECIMEN PREPARATION

The PC and PMMA materials were unchanged from those used in the previous study. Specimens were used as cut out of sheet stock, making sure that all burrs were removed. The standard specimen size was 25 x 25 x 12.5 mm. The other target materials are described below.

### 2.1 Polymethylmethacrylate

Specimens were cut from a single sheet of Type G Plexiglas<sup>®</sup> PMMA (produced by Rohm and Haas). Continuing with our former practice, the sheet was marked off in squares for cutting and a record kept so that the original location of each specimen in the sheet could be identified.

### 2.2 Polycarbonate

The PC resin was manufactured by the General Electric Company and is designated as Lexan<sup>®</sup> resin general purpose glazing sheet, Type 9034-112. A single sheet of 12.5 mm thick material was used, and specimens marked, and records kept as for the case of PMMA.

### 2.3 Epoxy

The epoxy specimens were of previous stock which was molded out of a mixture of 20% by weight of methylene dianiline with Epon<sup>®</sup> 828 resin manufactured by Shell Chemical Co. Resin was cast into a 12.5 mm slab, cured, and cut into 25 x 25 mm samples.

### 2.4 Inorganic Glass

A sheet of Pyrex<sup>®</sup> borosilicate glass 12.5 mm thick was cut into 25 x 25 mm samples.

### 3. IMPACT BAR STUDIES

The experimental arrangement has been briefly described in Section 1.1 and is in most details unchanged from that used in the previous contract effort. Complete details can be found in Reference 5. The general arrangement is shown in Fig. A. The main differences are the use of more advanced electronic instrumentation including a custom-built, low noise, wide band differential amplifier/Wheatstone bridge system and an improved digital storage oscilloscope Nicolet Model 2090-2, Explorer II. Other new details specific to the various classes of experiments are described below.

#### 3.1 PMMA BAR

3.1.1 Changes in Propagated Pulse Shape. In the previous report,<sup>(5)</sup> it was noted that the impact of a steel striker with the ideally elastic inorganic glass target resulted in a pulse that looked similar to the theoretically computed pulse, but which started and terminated much less abruptly. The observed peak maximum force and the pulse width at half peak height were 85% and 98.5% of the predicted values, respectively. However, the observed peak strain occurred at 52  $\mu$ sec instead of at 31  $\mu$ sec, and the actual pulse duration was 388  $\mu$ sec instead of the predicted value, 125  $\mu$ sec. When the experimental pulse was analyzed to yield the force penetration dependence, the results were at considerable variance with the well-verified Hertz law behavior. The pulse and the inferred force dependence are given in Figs. A and B.

The fact that substantial changes in pulse shape occurred as the signal passed down the impact bar was established by sensing the same stress pulse at three different stations along the impact bar length. The pulse was produced by striking a PMMA target, attached to the bar with the 4.5 mm diameter striker. One gage was a single gage embedded

in the bar on the center axis about 1.25 cm from the struck end. Hence, it sensed pulses while the wave fronts were still substantially spherical. It was located in a separate 2.5 cm bar segment, able to be acoustically coupled to the main bar, and is designated as the "detachable" gage. The other gages were actually pairs located 25 cm and 90 cm from the struck end on the outer surfaces of the main bar.

Fig. C shows that the leading edge (toe or nose) is indeed becoming less and less abrupt as the pulse travels along the bar. A more detailed description of the pulse at the detachable gage (1.25 cm) and at the 25 cm and 90 cm stations is given in Table A. The time ( $\mu$ s) needed for the pulse amplitude to rise 10% of its peak value increases in the sequence 18, 24, 35 at the three stations, respectively. That is, relative to the 10% reference mark noted for the first station, it requires 6  $\mu$ s longer to reach the same amplitude at the second station and 17  $\mu$ s longer at the third station. Inspection of the entries in the Table shows that at 30% of maximum peak the relative shifts remain essentially unchanged, being 5  $\mu$ s and 18  $\mu$ s, respectively. Similarly, for the maximum, the relative shifts are 4  $\mu$ s and 21  $\mu$ s. These values are identical within the experimental error, indicating that most of the pulse variation (on the rising side) occurs at or below the 10% peak, i.e., in the nose of the curve. However, the shift in the width of the pulse, at half the peak height, indicates that the decreasing part of the pulse is fanning out as the pulse travels. The small decrease in the area of the pulse between the 25 and 90 cm sensor locations as measured by  $(A \times t_{0.5})$  indicates that attenuation losses are insignificant.

Additional evidence of the change in pulse shape is seen for the cases of two rather different kinds of impact. In one experiment a 1.25 cm thick square of glass was the target and was impacted with the 4.5 mm striker. In the other experiment, a crushable impact resistant

TABLE 3.1.1A  
TIME ( $\mu$ s) AND AMPLITUDE OF PULSE AT VARIOUS STATIONS

<u>Pulse Feature</u>	<u>Sensor Location</u>					
	<u>Detachable Gage</u>		<u>25 cm</u>		<u>90 cm</u>	
	<u>CR*</u>	<u>ET*</u>	<u>CR</u>	<u>ET</u>	<u>CR</u>	<u>ET</u>
1st Indication of Impact	0 $\pm$ 3	0	133 $\pm$ 3	0	437 $\pm$ 3	0
10% of Max.	18 $\pm$ 1	18 $\pm$ 4	157 $\pm$ 1	24 $\pm$ 4	472 $\pm$ 1	35 $\pm$ 4
30% of Max.	42 $\pm$ 1	42 $\pm$ 4	180 $\pm$ 1	47 $\pm$ 4	497 $\pm$ 1	60 $\pm$ 4
Max.	133 $\pm$ 3	133 $\pm$ 6	270 $\pm$ 3	137 $\pm$ 6	591 $\pm$ 3	154 $\pm$ 6
$t_{0.5}$ = Half Peak Ht. Duration	197		202		217	
A = Peak Amplitude**	123***		17.6		15.6	
A $\times$ $t_{0.5}$	2423***		3555		3385	

\*CR means Clock Reading; ET means Elapsed Time

\*\*Arbitrary Units

\*\*\*Should be multiplied by two to put on comparable basis with other values since only single gage is at this station.

layer applied to a SiC base was struck by a 19 mm diameter steel ball at about the same velocity. Thus, two sets of pulses were sensed as they passed the strain sensor 25 cm and 90 cm, respectively, from the place of impact and are shown in Figs. D and E. In addition, the behavior of the nose region for the pulse obtained with glass is given in Fig. F. These figures show shape changes in both cases. The pulse for glass becomes less steep in the nose region as it travels down the bar and becomes more extended in the tail region. These shifts in pulse shape are also shown in the following table, which quantifies the pulse geometry at various points. As before, the times required for the pulse to rise to 10, 30, and 100% of its maximum value are longer for the pulse sensed at the 90 cm station. The pulse area again appears to be only slightly diminished as the pulse travels along the bar between the two sensor locations.

In the case of the pulse obtained with the crushable material, note that at the 25 cm position there are two distinct maxima. The first peak is believed due to the collapse of the layer under impact, and the second corresponds to unloading due to rebound. However, in the pulse detected at the 90 cm station, this first peak is absent and is only suggested by a hint of a shoulder.

This overall evidence supports the hypothesis that the discrepancy between the observed and the predicted pulses and force displacement relations can be, at least in part, attributed to dispersion effects. However, making the necessary corrections is complex. This requires knowledge of the velocity-frequency dependence (which is also a function of bar shape). It also requires an analytical procedure for making the required corrections. As discussed in the preceding report, Fourier analysis is primarily useful for describing regular periodic or finite

TABLE 3.1.1B  
TIME (μs) AND AMPLITUDE OF PULSE AT VARIOUS STATIONS

<u>Pulse Feature</u>	<u>Sensor Location</u>			
	<u>25 cm</u>		<u>90 cm</u>	
	<u>CR*</u>	<u>ET*</u>	<u>CR</u>	<u>ET</u>
1st Indication of Impact	-36±3	0	272±3	0
10% of Max.	-8±1	28±4	304±1	32±4
30% of Max.	0±1	36±4	320±1	48±4
Max.	42±3	78±6	362±3	90±6
$t_{0.5}$ = Half Peak Ht. Duration	82		87	
A = Peak Amplitude	28.03		23.93	
A × $t_{0.5}$	2298		2082	

\*CR means Clock Reading; ET means Elapsed Time

processes. However, an impact pulse does not meet these criteria. Hence, the use of Fourier series to analyze a pulse into constituent frequency components involves unavoidably arbitrary procedures which unfortunately affect the answers to some extent. Fourier integral techniques would be preferable but are less well developed.

The difficulties associated with this approach led finally to replacing the PMMA impact bar in favor of an aluminum bar, dispersion effects in metals being much less pronounced than in polymers. However, quantitative dispersion data were obtained which may provide insight into the PMMA material itself. This is presented in the next section.

3.1.2 Dispersion Observations. The appropriate elastic constant to use to predict the sound propagation velocity down a bar depends on the relative transverse bar dimension compared with the wavelength (frequency) of the acoustic component of interest. When the wavelength is relatively large, the Young's modulus E is the appropriate quantity. When the wavelength is small, the plate modulus B defines the velocity. Since  $B/E = (2 + 2\nu + \nu^2)/(1 + \nu)$  where  $\nu$  is the Poisson ratio, in the case of PMMA this translates into a corresponding ratio of velocities of 1.46:1 due to geometric considerations alone. In addition, the PMMA has an intrinsic dependence of velocity on frequency relatable to its characteristic relaxation modulus behavior. The cross-sectional dimension of the bar, 1.9 cm, considered as a wavelength corresponds to a frequency of about  $10^5$  Hz. Since the typical pulse component frequencies as computed by Fourier analysis lie in the range  $10^3$  to  $10^6$  sec $^{-1}$ , a strong velocity-frequency dependence can be expected in the PMMA bar.

An experimental determination of the dispersion was planned by measuring the peak shape from the same impact event at two successive stations along the bar. However, since an impact between glass and a spherical steel striker can be accurately modeled with considerable confidence, the procedure selected was to compare the Fourier analysis of an observed pulse

at a known position from the impact site with the corresponding analysis of the theoretically computed pulse, keeping the arbitrary pre-pulse and post-pulse zero signal duration fixed. The theoretical pulse can be represented as a sum of Fourier components each of which has the form:

$$A_0(n) \sin [2\pi\omega_0 n t_0 + \theta_0(n)]$$

in which  $n$  is the order of the harmonic,  $A_0$  is the amplitude of the  $n$ th harmonic,  $2\pi\omega_0$  is the inverse of the time duration of the total pulse (including pre-pulse and post-pulse considerations), and  $\theta_0(n)$  is the phase angle. The pulse, experimentally observed at a station a distance  $L$  from the struck end, can be similarly described as the sum of components of the form:

$$A(n) \sin [2\pi\omega n t + \theta(n)]$$

The periods are chosen to be identical, i.e.,  $\omega = \omega_0$ . The times  $t$  and  $t_0$  refer to independent "clock" readings, each started when a signal was first detected at the struck end and at the strain gage. The time for the Fourier component to travel from the struck end to the gage is  $L/c(n)$ ; where  $c(n)$  is the sound velocity in cm/sec for the  $n$ th harmonic. For the case at hand, the distance  $L$  has the value 30.5 cm. The times  $t$  and  $t_0$  are related by  $t_0 = t - (L/c(n))$ , and the change in phase angle due to this travel is  $2\pi\omega_0 n L/c(n)$ . This difference in phase angle is obtainable from the Fourier analyses =  $\theta_0 - \theta$ . Thus,  $c(n)$  can be computed and is proportional to  $n/(\theta_0 - \theta)$ . These quantities are given in Table A. However, the reliability of the values of  $\theta_0$  and  $\theta$  from the Fourier analysis can be expected to decrease with increasing values of  $n$ , because the noise in the pulse signal will tend to mask the true pulse shape. Furthermore, it becomes increasingly difficult to make an unambiguous assignment

TABLE 3.1.2A  
COMPARISON OF FOURIER COMPONENTS FOR AN ACTUAL AND A THEORETICAL  
IMPACT BETWEEN A STEEL BALL AND A GLASS TARGET

Order of Harmonic n	Amplitude		Phase Angle		$\frac{\theta_0 - \theta}{n}$
	Theory $A_0$	Expt. A	Theory $\theta_0$	Expt. $\theta$	
0	$2.72 \times 10^{-4}$	$3.12 \times 10^4$	$\pi/2$	$\pi/2$	----
1	2.43	2.56	.660	.254	.406
2	1.73	1.72	-.170	-.860	.345
3	1.03	$8.60 \times 10^{-5}$	-.805	-1.831	.342
4	$6.21 \times 10^{-5}$	3.90	-1.185	-2.597	.353
5	4.13	2.06	-1.503	-3.033	.306
6	-2.66	-1.05	1.382	-.467	.308
7	-1.86	$-4.62 \times 10^{-6}$	1.231	-.641	.267
8	-1.33	-2.23	1.045	-1.011	.257
9	$-9.44 \times 10^{-6}$	-1.40	.955	-.744	.188
10	-7.40	-1.11	.854	-1.057	.191

of the value of  $\theta_0 - \theta$ , because  $\sin \theta$  is not a single valued function of  $\theta$ . Assignments judged to be reliable were made for the first ten harmonics leading to the deduced dependence of velocity on frequency as follows:

<u>Harmonic</u>	<u>Frequency</u> <u>KHz</u>	<u>Velocity</u> <u>(Obs)</u> <u>m/sec</u>	<u>Velocity</u> <u>(Reported)</u> <u>m/sec</u>
1	2.3	1690	2034
2	4.5	2000	2059
3	6.8	2020	2073
4	9.1	1960	2083
5	11.3	2260	2091
6	13.6	2250	2098
7	15.9	2590	2103
8	18.2	2690	2107
9	20.4	3680	2111
10	22.7	3620	2115

From this it can be seen that the rate of change of velocity with increase in frequency even over the first 8 harmonics is 14 times greater than the change expected only on the basis of the intrinsic material properties (relaxation modulus).

A similar examination of the ratio of the amplitude of the experimental to the theoretical pulse suggests that there is little attenuation of the first two harmonics, but that there is a nearly linear decrease in relative amplitude persisting at least down to the 8th harmonic (18.2 KHz) at which level little further change occurs. This is shown in Fig. A. However, the calculated 85% diminution in amplitude stands in contrast to the observed relatively low attenuation of the overall pulse as discussed in Section 3.1.1. Therefore, the assumption of independent, non-interacting propagation of the constituent Fourier components of the impact pulse

warrants further critical examination. These observations indicated that applying the necessary corrections to the detected pulses in a PMMA impact bar will be difficult. However, analyzing these changes in pulse shape may be a useful tool for investigating the high frequency, moderate-to-high stress responses of polymers under conditions of distributed loading.

### 3.2 Aluminum Impact Bar

Among the commonly available metals, aluminum offers a relatively low acoustical impedance, high elastic compliance, and a sufficiently high yield stress to ensure that it will respond elastically over the stresses likely to occur in an impact bar under the anticipated conditions. Furthermore, aluminum is not expected to exhibit much intrinsic dispersion. However, geometric factors such as discussed in Section 3.1.2 can cause dispersion. The transition frequency between plate-like and rod-like sound propagation in an aluminum bar is a factor of 3 greater than for a PMMA bar of the same lateral dimensions. However, because the Young's modulus of aluminum is more than an order of magnitude greater than that for PMMA, for a given size bar and reaction force the strain is proportionally smaller. Hence, to detect the pulse produced by the impact with no loss in relative precision requires either more sensitive strain detectors or higher gain low-noise amplification. Finally, because of the greater sound velocity, the time between pulse reflections from the bar ends is correspondingly shorter. Thus, there is less time available to observe the post pulse signal following the rebound of the striker from the target. In principle, this should be a regime in which the strain remains zero. However, in practice there is always some damped oscillatory tail to the strain pulse signal.

3.2.1 Description of the Aluminum Bar Apparatus and Alignment Procedures. The bar consists of a 180 cm long bar of 2024-T351 alloy aluminum in the form of a 19 mm diameter cross-section rod. The ends

were cut perpendicular to the rod axis, and a pair of SR-4 silicon semiconductor strain gages mounted 11.4 cm from the struck end. The electronic instrumentation is unchanged from that used with the PMMA bar. In order to eliminate the post-pulse ringing, great pains were taken to ensure that the bar was horizontal, that the point of impact was on the axis of the bar, and that the striker motion was in a plane containing the bar axis. This was accomplished by use of a carefully calibrated cathetometer which rotated around a vertical axis to ensure that the bar was initially horizontal and that the striker made contact at the center-line height of the bar. Two plumb lines, one at each end of the bar, defined a vertical plane. The bar axis was adjusted to lie in this plane by means of the thin wire bifilar supports at the 1/4 and 3/4 positions along the bar length. The striker was similarly adjusted so that its center of mass lay in this same plane at the point of contact and swung in this plane as it was pulled from its rest position.

A long, thin thread attached to the striker was used to displace the striker to its initial position. The height of the striker above the point of contact was determined by means of the cathetometer and was used to calculate its impact velocity. The rebound position was determined photographically. By maintaining the camera lens open, shining a bright light on the striker, and noting on a Polaroid<sup>®</sup> picture where the maximum rebound occurred, it was possible to relocate the striker to this position. This was done by pulling the striker with a thread until its position as viewed through the camera reproduces the position shown in the photograph. The height was then determined using the cathetometer, allowing the rebound velocity to be determined. Thus, the momentum of the striker was completely defined.

The momentum imparted to the impact bar was determined from the displacement of a small rider along a fine wire support which was beneath the bar and oriented parallel to it. A X-Y cathetometer was used to determine the maximum displacement of the rider and, hence, of the bar. This allowed the velocity of the bar, as a result of the impact, to be determined.

The strain gages and electronic amplification system were directly calibrated by deadweight loading of the bar at two load levels. The strain gages were calibrated by the supplier. Furthermore, in each run, in effect another calibration was performed by making use of the fact that the time integral of the pulse strain must equal the measured net momentum of either the bar or the striker. Further details may be found in Sections 3 and 4 of the preceding report.

3.2.2 Critical Testing of the Bar Apparatus. The force-time pulse due to an impact of an elastic spherical projectile against an elastic planar specimen mounted on the end of an elastic bar can be accurately computed if the elastic properties, dimensions, masses of all of the bodies are known, plus the initial velocity of the striker. By this means known pulses were produced using a hardened steel 19 mm diameter ball bearing weighing 28.3 g as the striker. Glass, and also hot-pressed silicon carbide blocks, having thicknesses of 12.5 mm served as the elastic specimens. These were mounted on the ends of the aluminum impact bar.

The comparison between the computed and experimentally observed pulse when the above striker collides with glass and hot-pressed SiC targets at 1.77 m/sec is shown in Table A.

These results show that the observed pulse at the strain gage 12.7 cm from the site of the impact very closely follows the predicted behavior. Detailed examination of the toe and tail regions of the pulse reveal that the observed pulse builds up more slowly in the toe region than is predicted

TABLE 3.2.2A  
IMPACT CHARACTERISTICS

Young's Modulus (GN/m <sup>2</sup> )	Glass		SiC	
	69 Obs.	Theory	440 Obs.	Theory
Rebound Velocity (m/sec)	1.08	1.08	.85	.85
Max. Force (Kg)	182	184	260	246
Time at Max. (μsec)	39	36	29	24
Pulse Duration (μsec)	85	83	62	58
Pulse Width at Half Max. Force (μsec)	46	45	29	30
Sound Velocity of Bar	5100 m/sec			
Young's Modulus " "	71 GN/m <sup>2</sup>			
" " of Striker	200 GN/m <sup>2</sup>			
Initial Velocity of Striker	1.77 m/sec			
Diameter of Striker	19 mm			
Mass of Striker	28.3 g			

by the model. Hence, taking the first indication of an increase in detectable strain in the pulse as the time corresponding to contact between the striker and the target, results in a pulse in which the main portion is displaced towards greater times. This shift persists over the entire pulse. Figs. A and B show the shift of the toe and tail region relative to the theoretical pulse for glass, and Figs. C and D give similar information for SiC.

Several mechanisms or combinations thereof could be responsible for this shift. If the acoustic impedance match between the bar and the specimen is not perfect, then partial reflection of strain pulse will occur at the plane of attachment. This should have the effect of putting a buffer, somewhat analogous to inductance in an electric circuit, between the specimen and the bar. Hence, there will be a lag in the build-up of the total signal, which should be related to the transit time for a pulse to travel through the specimen thickness and the impedance mismatch. A second effect is attributable to acoustic dispersion. Even for an aluminum bar of 19 mm diameter, a transition from plate-like to rod-like sound propagation will occur at frequencies of the order of  $3 \times 10^5$  Hz. Since the theoretical pulse for glass and SiC rises significantly over a time period corresponding to this frequency, it follows that the pulse contains appreciable contribution from frequencies greater than this transition value. This effect will be more pronounced for the case of SiC relative to glass. The high frequency contributions will propagate faster than the low frequency ones. Hence, these could provide "advance notice" of the arrival of the pulse in the form of a toe. If so, for the present case, taking into account the difference in velocity of the two modes of sound propagation, could result in a toe of up to 4  $\mu$ sec in the case of the aluminum with the strain gage 12.5 cm from the impact site. For comparison, a

toe up of 43  $\mu$ sec is predicted possible for the PMMA bar with the sensor 25 cm from the impact site. Other contributing effects are also possible.

At this time, while not proven, the evidence suggests that the dispersion effects are largely responsible for the extended signal in the toe region. In the case of the aluminum bar, this effect appears to perturb the pulse shape only slightly. This perturbation does affect the force-penetration dependence computed from the pulse. The extended toe is interpreted as additional projectile penetration. Hence, during the 2.3  $\mu$ sec shift noted for the case of glass at an impact velocity of 1.77 m/sec, the striker moves 4  $\mu$ m, whereas in the case of SiC the shift is 6  $\mu$ sec and the striker moves 11  $\mu$ m. This is shown in Figs. E and F. The computed force-penetration behavior using data from a similar experiment, but in which the glass specimen is mounted on the PMMA bar, is shown for comparison.

These validation experiments show that impact pulses obtained on the aluminum bar, except for an artifact associated with the toe, are excellent representations of the actual force history at the site of the impact. Furthermore, the effect of the artifact, while very pronounced in the case of an impact with an extremely hard material such as silicon carbide, is already reduced when the target is glass, a material only one-sixth as stiff. When polymers are the target material, the effect is expected to become further diminished. These results provided the level of confidence needed to proceed with impact measurements on the polymeric materials of primary interest, with reasonable assurance that the derived data will have physical significance.

### 3.3 Impact Measurement Results

Impact determinations were made on PC, PMMA, and epoxy standard specimens at two impact velocities and using two different strikers, the 19 mm diameter, 28.3 g one, and the 4.5 mm diameter, 42 g one. In addition, the calibration/validation runs, described in the preceding section, on glass and hot-pressed silicon carbide are included for comparison. The pulses were recorded by means of the digital storage oscilloscope. Individual data points, usually at 1  $\mu$ sec intervals, were read into a computer file for subsequent processing. About twenty data points just ahead of the pulse were included to define the initial zero strain base line. The pulse data were recorded up to the time where the reflected pulse occurred. Some duplicate runs were made. However, the reproducibility was such that this was later considered to be unnecessary, except where there may have been some question about the experimental details. Software programs previously developed were used to compute reaction force, penetration depth, momentum transfer, energy transfer, etc. A detailed discussion of the basis of these calculated quantities can be found in the previous report, and a summary is given in the Appendix.

An example of the notation for identifying the various separate determinations is PM/19/1.77. The letters identify the target material (PM = PMMA, PC = PC, Ep = Epoxy, G = glass, and SiC = silicon carbide). The number between the slashes refers to the striker diameter in mm, and the final number is the impact velocity in m/sec. Duplicate runs, if any, are indicated by lower case letters, a, b, etc.

The results for these materials are summarized in Table A. Plots of the stress pulse and of the derived force versus penetration, local work versus penetration, and penetration versus time are given in Figs. A-P. *A priori* the force versus penetration behavior

TABLE 3.3A  
SUMMARY OF EXPERIMENTAL IMPACT RESULTS

	$F^*$	$X^*$	$t$	$X_f$	$\frac{W}{X_f}$	$\frac{W}{K.E.}$
	Maximum Force 1bs	Maximum Penetration mils	Pulse Duration $\mu$ sec	Non-Recover Local Work ERGS $\times 10^{-5}$	Exit Depth @ Zero Contact mils	$\frac{X_f}{X^*}$
PM/19/1.77a,b	196, 197	3.86, 4.04	183, 186	.448, .454	.25, .41	.07, .1
PM/19/2.93	357	5.89	167	1.47	.59	.10
PM/4.5/1.77	160	6.85	330	1.95	.77	.11
PM/4.5/2.92	284	10.7	304	6.29	2.34	.22
PC/19/1.77	146	5.75	263	.387	.19	.03
PC/19/2.93	266	8.13	231	1.33	.28	.03
PC/4.5/1.77	115	9.84	471	2.35	1.15	.12
PC/4.5/2.90a,b	199, 199	15.0, 15.4	424, 424	7.65, 7.68	3.75, 4.27	.25, .28
Ep/19/1.77	159	4.93	227	.885	.64	.13
Ep/19/2.93	293	7.20	203	2.24	.82	.11
Ep/4.5/1.77	133	8.2	400	2.09	.83	.10
Ep/4.5/2.92	232	13.0	382	6.39	1.70	.13
G/19/1.77a,b	407, 402	17.1, 17.2	84, 85	-.003, -.002	.23, .22	.13
Sic/19/1.77	574	1.36	62	-.11	.41	.30
					0	0
					0	.01

would be expected to relate to the results previously obtained using the mechanical test machines. However, in the present case, the penetration velocity is not constant. The local work versus penetration is the total energy extracted from the striker minus the energy contained in the stress pulse that is traveling down the impact bar. Hence, it represents the work that remains in the specimen itself. Some, but not necessarily all, of this stored work is used to cause the striker to rebound. Hence, part of the work is non-recoverable. The amount of the local work, at any given penetration depth, assignable as being irreversible is the accumulated difference in the work recovered during the exit trajectory less that done during penetration. If relaxation effects are neglected, this provides a measure of the visco-plastic work done on the specimen.

The plots of penetration versus time provide information of the relative motion of the striker and provide a means of relating the free impact response to the motions imposed by the mechanical test machines in our prior work.

### 3.4 Commentary on Pendulum Impact Results

Table 3.3A shows, as expected, that the larger diameter striker penetrates less and does less damage at a given velocity than does the smaller striker. This is not unexpected. In most respects, such as maximum force, pulse duration, and penetration depth, the results for epoxy were intermediate to those for PC and PMMA. The one exception was in the level of irreversible work absorbed by the epoxy during impact from the larger ball. Almost twice the level of work was retained as would be estimated from the other regular behavior. The runs Ep/19/1.77 and Ep/19/2.93 were each made with separate fresh specimens. However, the epoxy was mixed and hand cast in the laboratory, and it is possible that the material is not as uniform as the

other commercial resins. Therefore, some caution is recommended before attaching major significance to this particular observation.

A computation of particular interest is the penetration depth at the time that the strain gage registers zero strain. In the case of elastic materials, there should be complete elastic recovery and, hence, a reaction force until the penetration depth is zero. The penetration depth is one of the more complicated quantities to compute. It represents a difference between two large terms, less a smaller correction term for the contraction of the impact bar. For this reason, the reliability of this quantity can be questioned. However, the quality of the pulse data with respect to noise level and the various internal checks suggest that this quantity is either real or is a good measure of some related systematic effect. If the exit depth  $X_f$  is taken as the instantaneous equilibrium impact crater depth, then this would be expected to increase in a regular way with increase of maximum penetration depth  $X^*$  and with the non-recovered work  $w$ . The regular behavior of  $X_f/X^*$  and  $w/X_f$  add further confidence to the physical reality of the computed value of  $X_f$ . However, absolute verification would require further experimentation to directly measure this quantity.

### 3.5 Ballistic Impact Using Air Gun

The next velocity regime to be studied requires the use of a gun to drive the projectile against the target. A preliminary experiment was undertaken to determine what new elements may be introduced in this work. A 4.5 mm diameter ball bearing was used as the projectile in an air gun and fired at 85 m/sec against a standard PMMA target mounted on the end of the impact bar. The pulse and bar momentum were measured in the usual way. The information is summarized in Table A and in Figs. A-1 to A-4. The most distinguishing features from the experiments

described in Section 3.3 are the short contact time (26  $\mu$ sec) and the rather considerable ringing after the projectile has left the specimen. This is shown in Fig. A-1. The abruptness of the pulse suggests that the same problems as discussed for the impact with glass and SiC in Section 3.2 having to do with the tapering-on of the pulse signal in the toe region are probably operative here as well. Note that for a projectile traveling 85 m/sec, an error of 1  $\mu$ sec in the time corresponds to a distance traveled of  $85\mu$  (3.3 mils). Assuming a time shift (due to the taper-on effect) of the same magnitude as for the silicon carbide pulse, suggests that the calculated maximum penetration and the depth at the moment of projectile separation are overstated by about 20 mils (500  $\mu$ m). Clearly an uncertainty of such a magnitude precludes a straightforward interpretation of the computed force versus depth behavior given in Fig. A-2. The slope at large apparent depth appears reasonable. Hence, in future work, additional experimental means of eliminating the taper-on portion of the pulse and/or some way of correcting for this must be found. As may be recalled, this effect is believed to be an artifact attributable to acoustic dispersion.

TABLE 3.5A  
IMPACT PULSE DATA

Target	PMMA
Projectile	4.5 mm dia., .371 g
Impact Velocity	85.4 m/sec
Rebound " (calc.)	52.2 m/sec
Max. Force	405 Kg
Time at Max.	18 $\mu$ sec
Pulse Duration	26 $\mu$ sec
Pulse Width of Half Max. Force	14 $\mu$ sec
Calc. Max. Penetration	40.4 mils (1026 $\mu$ m)
Calc. Depth at Time of Specimen/Projectile Separation	26.9 mils (683 $\mu$ m)

#### 4. HIGH SPEED CINEMATOGRAPHY OF THE IMPACT PROCESS

Our earlier studies<sup>(3,4)</sup> noted the development of a clear, optically distinct, lens-like region under the spherical indenter/striker as it was driven into PC, PMMA, and epoxy specimens. This region is believed to consist of densified resin. Using a 4.5 mm sphere driven into the polymer at 1.2 mm/min, it was possible to follow the time-wise development of the densified zone using motion picture photography. When the ball motion was stopped, this zone was observed to contract slightly. In another set of experiments, PC and PMMA were impacted by a 4.5 mm steel ball at velocities between 150 and 250 m/sec. Again, the densified zones were clearly visible within the specimens at the sites of the impact. In the case of PMMA, local cracking occurred as well at the upper end of the velocity ranges.

The most direct way to observe what happens during a high velocity impact is to be able to record it photographically at speeds which allow the various stages of the impact process to be resolved. A long range goal is to couple the photographic documentation with the simultaneous sensing and recording of the stress pulse. However, at this stage, the immediate objective was to be able to capture the details of the impact process, including the development of the densified zone, using a high speed motion picture camera. For this we had available a John Hadland Ima-Con framing camera capable of taking individual successive pictures at times as short as 1  $\mu$ sec. However, only about 10 complete pictures can be taken in a given experimental run. Hence, several problems had to be solved simultaneously, namely: (1) positioning the somewhat massive camera and optics relative to the air gun facility such that the impact region could be photographed full size; (2) providing a sufficiently high level of illumination and special

orientation to capture the densified zone and/or the development of cracks as they form; (3) synchronizing and timing the camera to capture the entire impact event in the 10 frames available. The apparatus and procedures are described next.

#### 4.1 The Experimental Arrangement

The Ima-Con camera is a device which transfers an image from a photodetector through a cathode ray tube to a phosphorescent screen from which the picture is made. Each image is approximately 16 mm wide x 19 mm high. A series of images are produced on the screen in the sequence shown on Fig. A by translation of the electron beam to new areas on the screen. The time from the start of one frame to the start of another is fixed by a plug-in electronic module and cannot be varied without changing the module. However, the number of frames per photographic exposure can be varied arbitrarily within limits. Since the dimensions of each frame do not change with the number of frames selected, they start to overlap at approximately eight frames per photograph. If the photographed object is restricted to an illuminated width of about 10 mm, a practical upper limit of 14 frames per photograph is reached. Even with high speed film (ASA 3000), a high-intensity strobe (Guide No. 90 at ASA 25) is required to illuminate the event at close range. Since exposure time varies directly with the time between frames, more illumination is required at higher framing speeds.

The appearance of the distorted zone beneath an indenter or an impacting projectile is apparently due to a difference in refractive index brought about by some combination of densification and polymeric configuration changes. While the zone is readily apparent to the eye which tends to time average images, it is not so apparent to the camera. However, the distorted zone could be revealed by pre-focusing the camera

on the exact point of impact. In addition, it was necessary to use back lighting, combined with collimation of the strobe light source, adjusted for maximum contrast at the zone boundary. This was achieved by precisely positioning an already impacted specimen at the point of impact, and making the necessary adjustments before replacing it with a fresh specimen.

Synchronization of the camera with the impact was accomplished by using the signal generated by the projectile as it passes through the second of two photoelectric detectors used to measure the impact velocity. That signal fires a strobe flash which in turn starts the camera.

Figure B is a schematic of the triggering circuit. The stop gate on the interval timer (gate 2) triggers a delay circuit which subsequently fires the strobe. Since it takes about 2000  $\mu$ s for the projectile to travel from the exit gate to the specimen and the impact event lasts only 50  $\mu$ s, it is clear that if a detailed photographic record of the impact is desired, very careful control of the triggering of the flash lamp and the camera is required. A photocell senses the strobe light and triggers the camera. (The first few images of each photo are usually underexposed at fast framing speeds since these frames are taken before the strobe lamp reaches full intensity.) The older (modified air rifle) compressed gas gun was used for these pilot experiments due to the large number of shots required in troubleshooting the procedure. This gun was found to be reproducible at 120 m/sec to  $\pm 1\%$ . The remaining link was to build a triggering circuit which had to interface both the interval-timer gate and the strobe light and be reproducible to  $\pm 5 \mu$ s.

#### 4.2 Experimental Results

Samples of PC and PMMA were impacted at 100 m/sec and 141 m/sec with a 4.5 mm steel ball. Figure A shows the impact of a 4.5 mm ball traveling at 140.5 m/sec on PC. There are  $\sim$ 5  $\mu$ s between frames. Of interest is the growth of the distorted zone to its maximum size during the course of the impact event and the subsequent decrease from the maximum during ball rebound. The sample was rephotographed several minutes later (Fig. B). The distorted zone is smaller than the maximum and appears better defined.

Figure C shows the similar event for PMMA. The results are also similar with the additional feature of crack formation during unloading. The crack is first clearly noticeable on frame #9. The distorted zone becomes very ill-defined in PMMA as the projectile leaves the sample and is almost impossible to rephotograph. Figure D is the best of a number of photographs of the distorted zone in PMMA taken after the impact event.

At the impact velocity of 100 m/sec, the disturbed zone in PC was smaller and less distinct, whereas in PMMA no photographic evidence for such zone formation was formed. However, visual inspection of the PMMA did reveal a very small distorted zone without crack formation.

The photographs also allow the impact velocity, recoil velocity, and contact duration to be measured. With a slower framing speed, e.g.,  $2.5 \times 10^4$  frames/sec, the ball could be imaged several times before and after the event as it traveled over a distance on the order of 1 cm from the specimen surface. The incident and rebound velocities,  $v_i$  and  $v_r$ , respectively, were calculated from this record.

Figure E shows a sequence taken at  $2.5 \times 10^4$  frames/sec with  $v_i = 140$  m/sec. The photograph magnification is determined from the apparent ball size. A strip of translucent paper is positioned behind the path of approach to clearly outline the ball. The distance from the nearest edge of the ball to the specimen surface ( $x$ ) is determined to  $\pm 0.1$  mm with a

precision rule and a magnifying eyepiece. Table A shows the data associated with Fig. E. The velocities and residence times are listed in Table B.

It should be noted that the specimens were coupled to essentially rigid metal blocks which did not translate as a result of the impact. The duration of the impact is partly determined by the nature of the specimen support. Therefore, only these four tests were made as a preliminary to assembling the entire system (i.e., the Hopkinson bar, the Ima-Con camera and the compressed gas gun). However, some qualitative observations can be made from the data in Table A. (1) The residence time of the ball on the sample varies inversely with incident velocity. (2) The rebound velocity increases with increasing incident velocity. (3) The residence time is ~50% shorter on PMMA than on PC under these conditions. If these materials behaved elastically, the ratio of the residence time should be inversely proportional to the Young's modulus to the 0.4. For the present case, this would be ca. 0.74. Hence, the PC has an effective modulus appreciably less than the value ( $2.79 \text{ GN/m}^2$ ) determined from sonic velocity measurements in the megahertz range. These tests demonstrated that the photographic techniques were adequately developed to the point where they can probably be used in conjunction with the impact bar.

TABLE 4.2A  
VELOCITY/POSITION DATA FOR THE IMPACT EVENT  
ON PMMA SHOWN ON FIG. 4.2E

---

Photo Calibration: 4.8 mm/cm

$t_f: 4 \times 10^{-5}$  sec

---

	Frame	x (mm) Photo	x (mm) Actual	v (m/sec)*
Arriving	1	----	----	----
	2	4.19	8.74	139.0
	3	1.52	3.18	----
Leaving	4	On Surface	----	----
	5	1.40	2.91	79.5
	6	2.92	6.09	79.3
	7	4.45	9.26	79.5
	8	5.97	12.44	----

---

$$*v = \Delta x / t_f$$

TABLE 4.2B  
VELOCITY/RESIDENCE-TIME DATA FOR PMMA AND PC

Material	$v_{\text{incident}}$ m/s	$v_{\text{rebound}}$ m/s	$t_{\text{residence}}$ $\mu\text{s}$
PMMA	99.1	64.3	29.0
PMMA	139.0	79.4	20.5
PC	101.8	53.6	49.5
PC	139.0	66.2	44.5

## 5. DISCUSSION

One of the central concerns of the present effort has been to solve the basic experimental problem of how to detect and then operate on an impact pulse so as to extract reliable materials response information. Ideally the information should mesh with and be of comparable accuracy to that obtainable from mechanical test machines. However, the nature of the directly observed information is quite different, so that some translation is required for comparison. The very good correspondence between the experimentally derived force-penetration depth relationship for glass, relative to the theoretically computed one, indicates that at least in the present pulse duration regime, the experimental procedures are adequate and the computational procedures are basically sound. Absolute equivalence between mechanical test machines and impact bar results is probably unrealistic, even in principle.

First, the basis for converting strain-time information into force versus depth is by means of one-dimensional elastic analysis. The occurrence of geometrically dependent dispersion is a consequence of the full three-dimensional elastic response of the impact bar. The solution of the transient response of a bar subjected to an end-on pulse using complete three-dimensional analysis is still an unsolved problem. Secondly, the local stress distribution within the specimen under dynamic loading cannot be identical with that under quasi-static loading, or where the sample is supported by a rigid, stress-reflecting solid. Hence, deviations from the classical Hertz law can be expected.

The force-penetration depth response, as determined by the present technique, suggests that the materials are responding in a more compliant way than was expected from the mechanical test machine behavior. This is illustrated in Fig. A which compares the response for PMMA using the 4.5 mm striker with the data obtained on the MTS machine at 100"/sec (2.54 m/sec) indentation velocity. However, as noted in earlier studies, under

conditions of deceleration, stress relaxation is accentuated, so that this will contribute to an apparently greater compliance than would be expected from constant penetration velocity experiments.

The impact data show that for a given set of impact conditions, the depth of penetration, the duration of the impact, and the irreversible energy absorbed by the specimen increase in the order PMMA < epoxy < PC. If the materials are analyzed in terms of the irreversible energy absorbed per unit distance of penetration, a pronounced geometric factor becomes evident. For the 19 mm striker, epoxy shows the greatest dissipation and PC the least. For the 4.5 mm striker, PMMA shows the greatest dissipation, and the remaining two materials are less but are relatively closely matched by this criterion.

At this point of our work, the most clearly distinguishing features that set PC apart from the other polymers studied are the greater extent of densification under the point of contact during penetration, its greater compliance, and the sensitivity to striker geometry of the irreversible work.

The large apparent depressions in the specimen at the time of striker/specimen separation need further effort to establish the validity of these results. Plausibility arguments have been presented for the case of the impacts with polymers. If true, then very appreciable anelastic deformation and recovery are involved in the impact process. Again, this is not unexpected from prior background work.<sup>(3)</sup> However, in the case of more abrupt impacts, such as with hard elastic specimens, or at higher velocities, artifacts affecting the pulse shape, presumably due to dispersion effects suggest caution.

In order to reduce or correct for the "taper-on" region at the leading edge of the pulse, several options are available. One is to correct the pulse shape, as was originally planned for the PMMA bar, using Fourier analysis and resynthesis. As noted the cross-over between

rod-like sound propagation and plate-like propagation, the latter exhibiting the greater sound velocity, occurs at a frequency  $\nu$  given approximately by  $\nu = c/d = \sqrt{E/\rho/d}$ , where  $E$  is Young's modulus,  $\rho$  density, and  $d$  diameter of the bar. Decreasing the diameter of the bar raises the frequency. The pulse would become planar sooner so that the strain gages could be brought closer to the struck end. Because of the shorter propagation distance, there would be less time spread in the signal due to dispersion. These procedures should help in getting a pulse of higher initial fidelity. Further improvement will require correction of the pulse shape. Analysis based on Fourier integral transforms would appear to offer the best procedure, in principle, providing that representations capable of subsequent resynthesis can be found.

## 6. ACKNOWLEDGMENT

The principal investigator appreciates the contributions of his collaborators and colleagues. The experimentation relating to the PMMA bar was performed by G.F. Selden, who also substantially contributed to the overall instrumentation facility. Dr. W.P. Minnear performed the difficult cinematographic studies. In addition, he is responsible for the improved aluminum impact bar apparatus and has been a partner in the measurements themselves and the data processing. Discussions with Dr. G.M. Roe and with R.L. Mehan have been consistently helpful.

7. REFERENCES

1. W.B. Hillig, "Impact Studies of Polymeric Matrices," General Electric CRD Report SRD-73-091, prepared under Contract N00019-72-C-0218 for Naval Air Systems Command, Dept. of the Navy, March 1973.
2. W.B. Hillig, "Impact Response Characteristics of Polymeric Matrices," General Electric CRD Report SRD-74-087, prepared under Contract N00019-73-C-0282, *ibid*, September 1974.
3. W.B. Hillig, "Impact Response Characteristics of Polymeric Matrices," General Electric CRD Report SRD-75-083, prepared under Contract N00019-74-C-0147, *ibid*, August 1975.
4. W.B. Hillig, "Impact Response Characteristics of Polymeric Materials," General Electric CRD Report SRD-76-112, prepared under Contract N00019-75-C-0320, *ibid*, September 1976.
5. W.B. Hillig, "Dynamic Impact Response Behavior of Polymeric Materials," General Electric CRD Report SRD-77-134, prepared under Contract N00019-76-C-0330, *ibid*, August 1977.

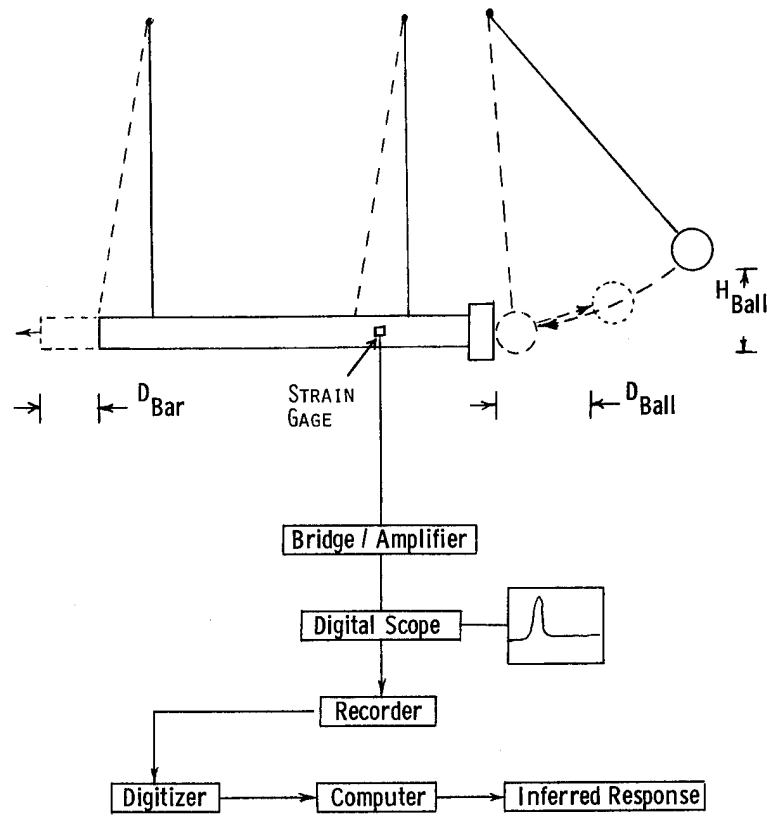


Figure 3A. Impact Apparatus

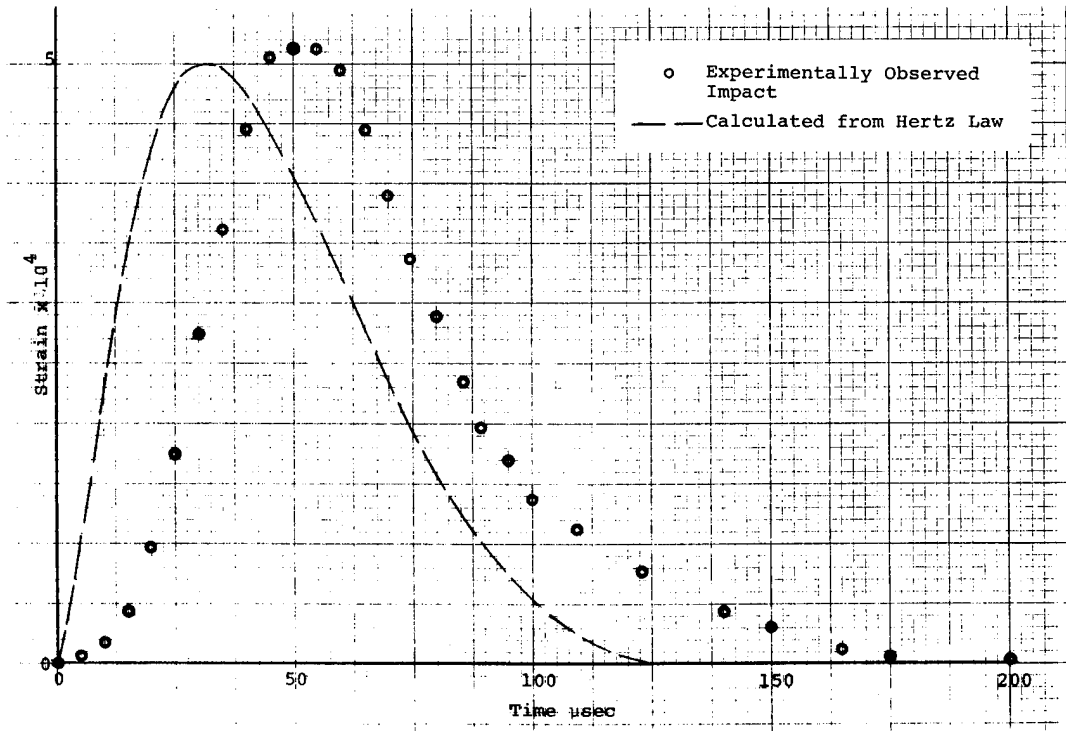


Figure 3.1.1A. Impact Pulse Due to a 19 mm Steel Ball Striking a Pyrex Target on a PMMA Bar

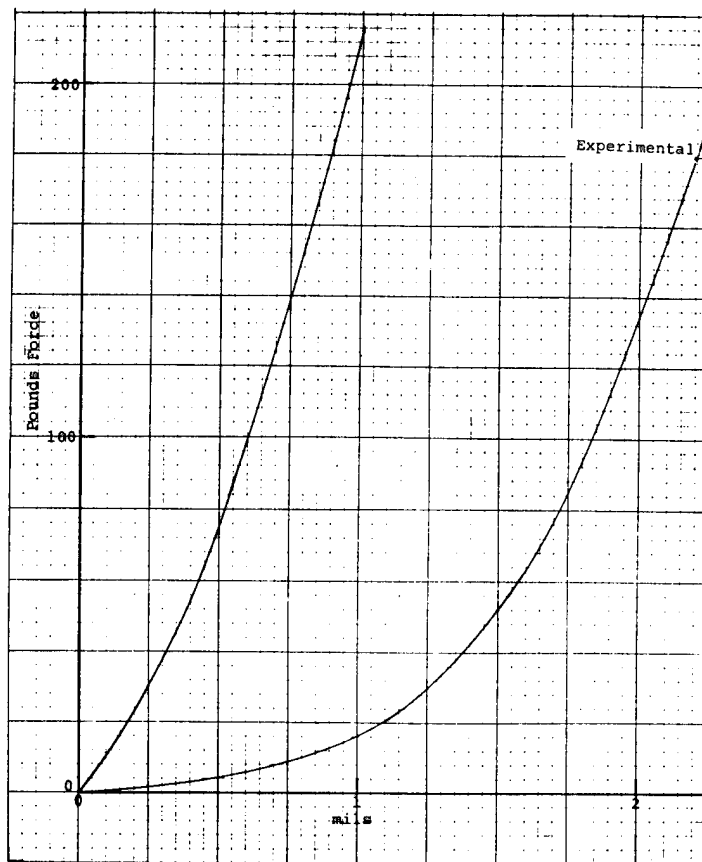
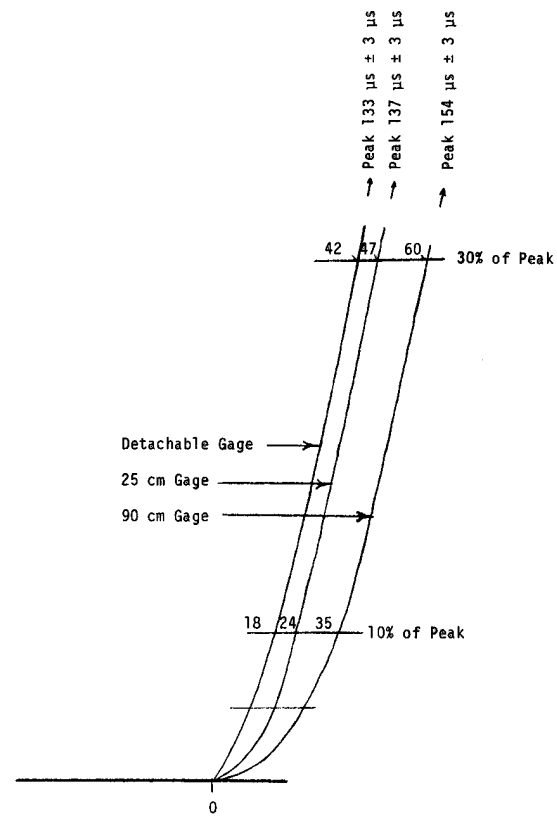


Figure 3.1.1B. Calculated Force Versus Penetration Depth Computed from Impact Pulse Using Glass Target; Experiment GL1N-1

Figure 3.1.1C. Detail of Nose of Impact Curve at Locations Indicated



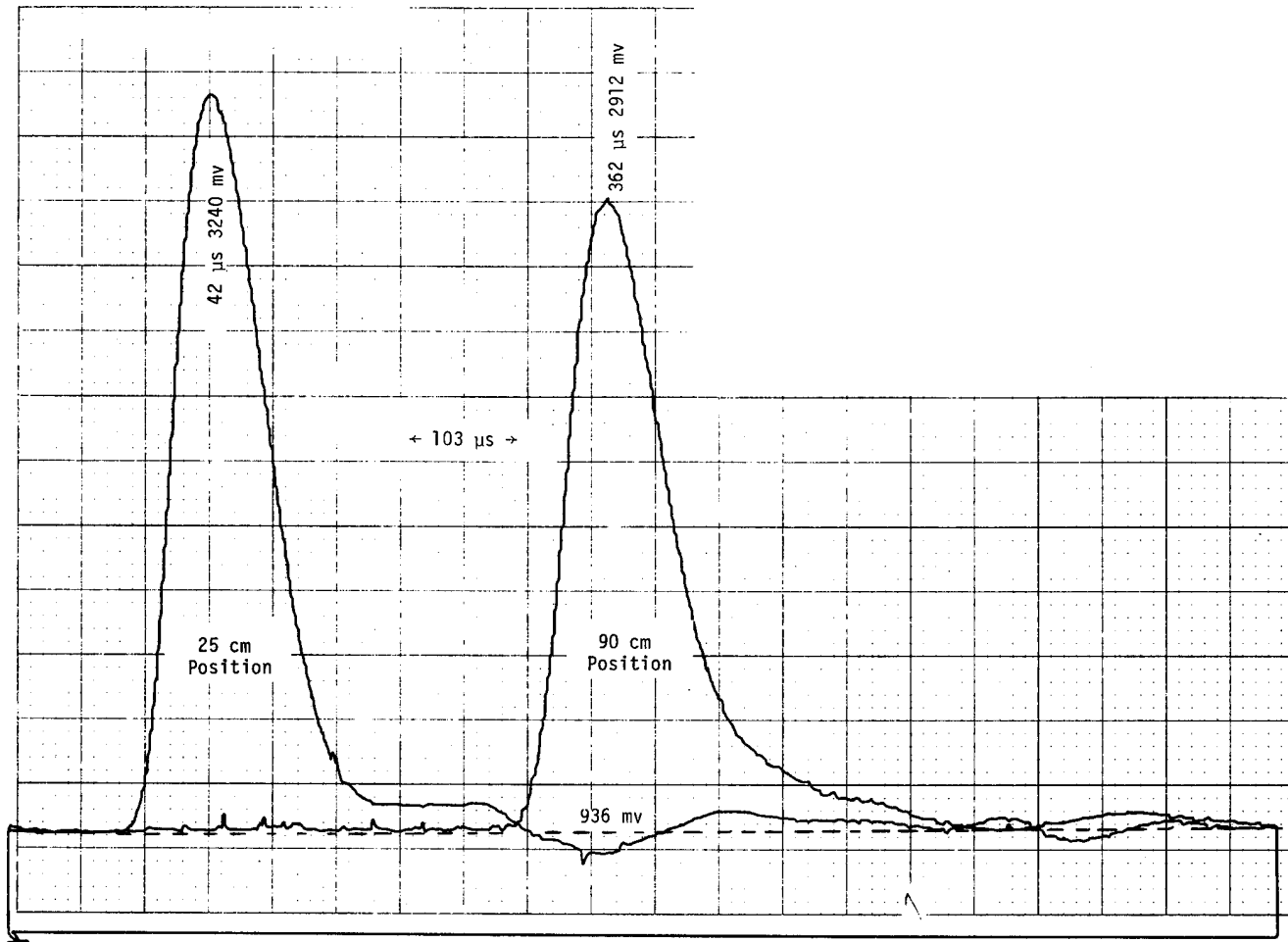


Figure 3.1.1D. Pulse Due to Impact Between 4.5 mm Striker and a Glass Plate Target as Detected at Two Stations Along Impact Bar

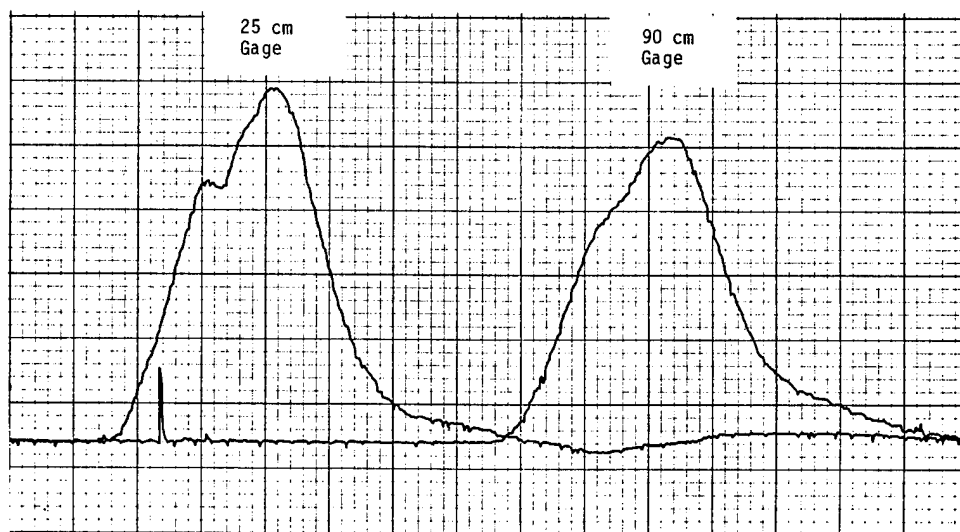


Figure 3.1.1E. Pulse Due to Impact Between 19 mm Steel Ball and a Crushable Ceramic Layer as Detected at Two Stations Along Impact Bar

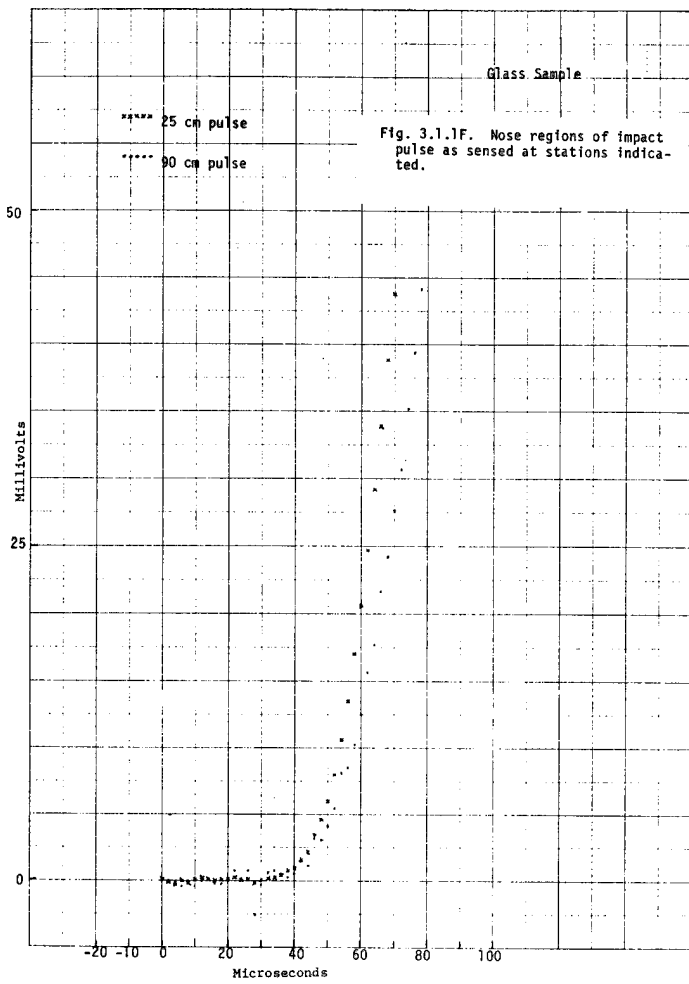
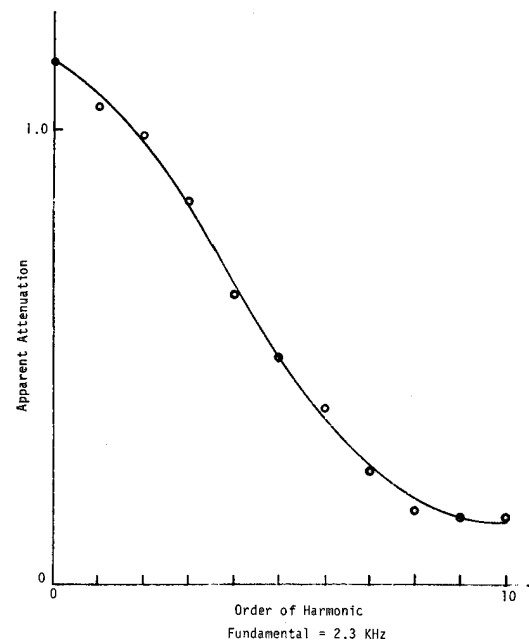


Figure 3.1.1F. Nose Regions of Impact Pulse as Sensed at Stations Indicated

Figure 3.1.2A. Deduced Acoustic Behavior of PMMA Bar



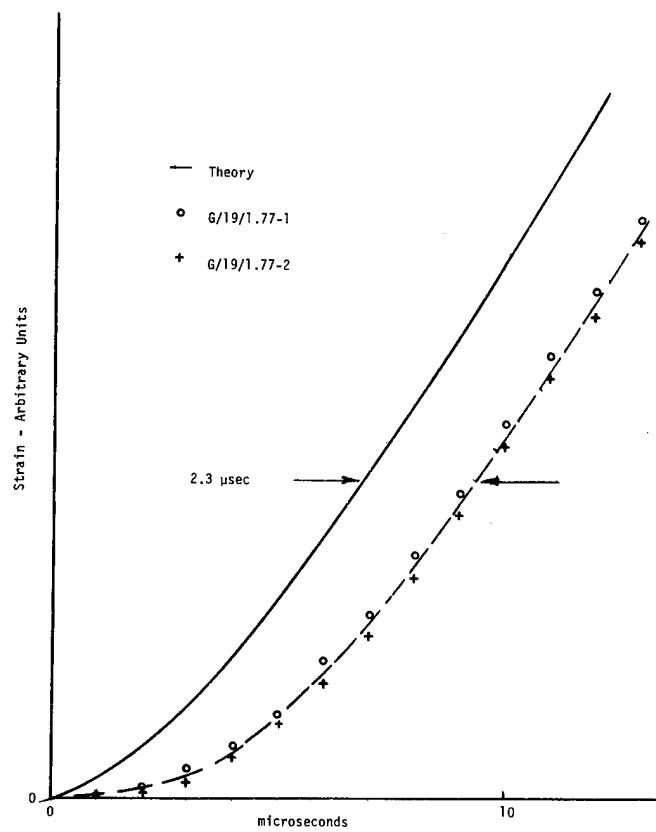


Figure 3.2.2A. Initial Portion of Strain Pulse for Glass

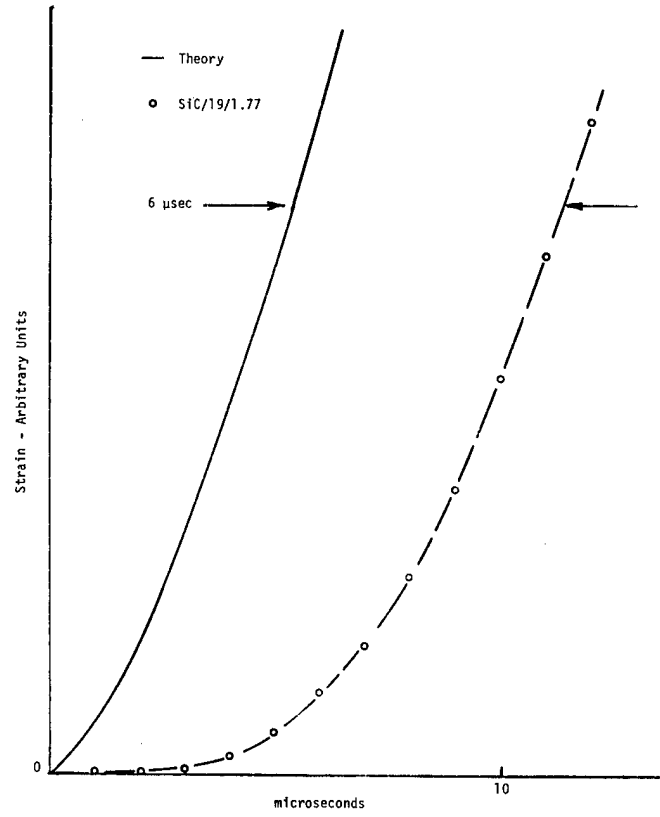


Figure 3.2.2B. Initial Portion of Strain Pulse for Silicon Carbide

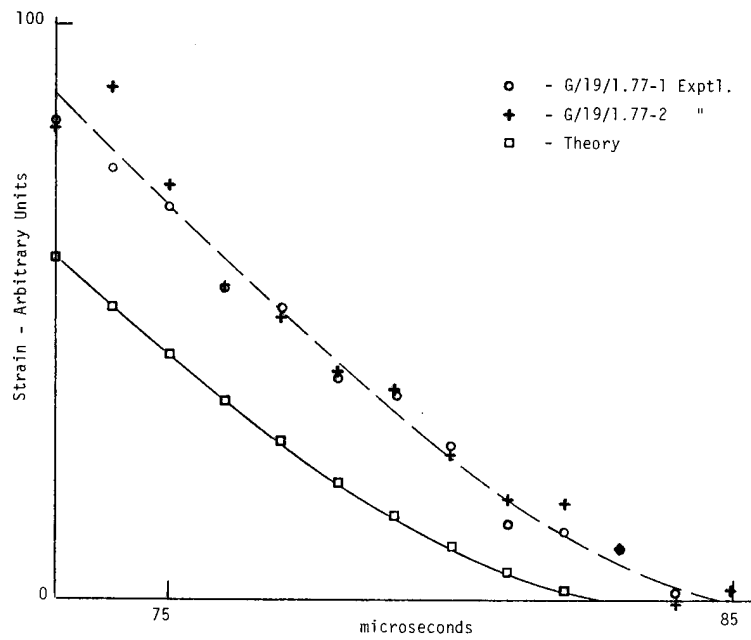
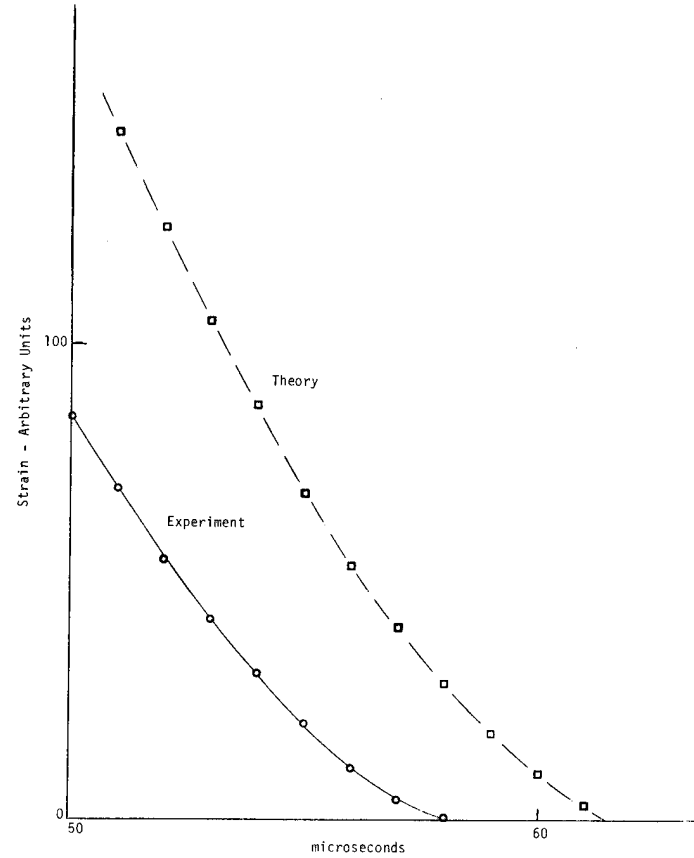


Figure 3.2.2C. Tail Portion of Strain Pulse for Glass

Figure 3.2.2D. Tail Portion of Strain Pulse for Silicon Carbide



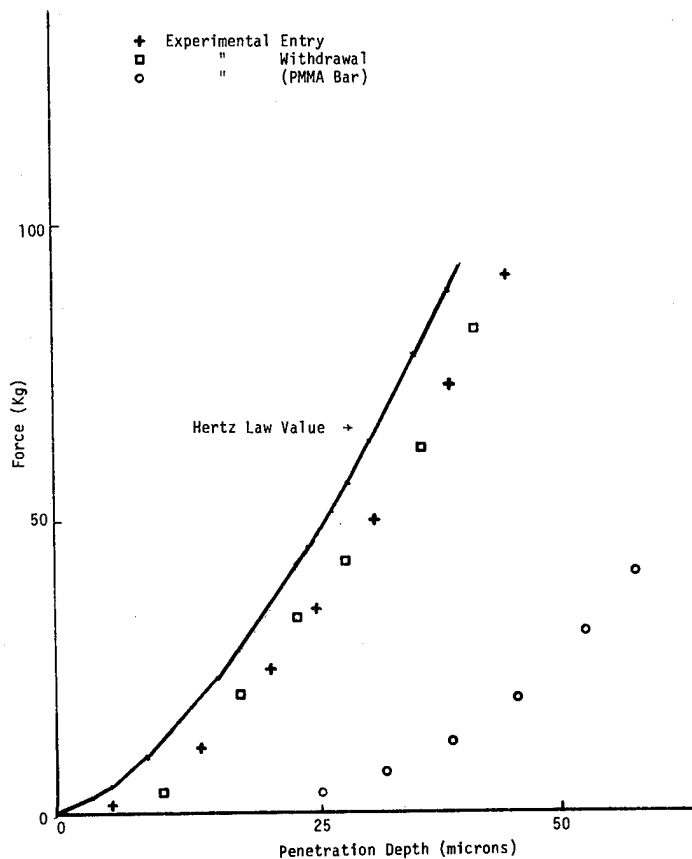


Figure 3.2.2E. Calculated Force Versus Penetration Depth for Glass

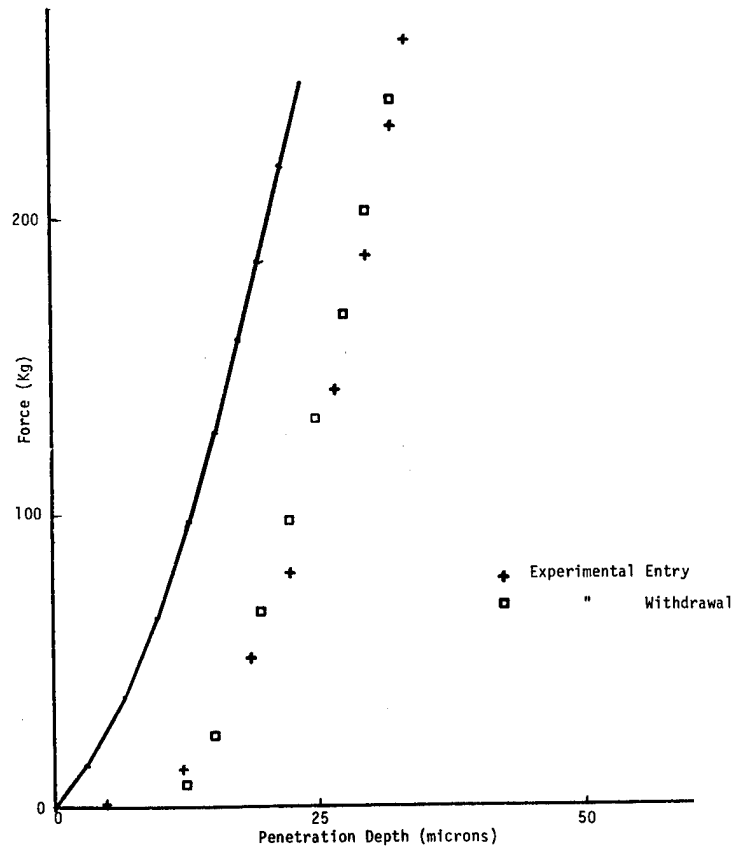


Figure 3.2.2F. Calculated Force Versus Penetration Depth for Silicon Carbide

Figs. 3.3 A through P  
&

Fig. 3.5 A

(I & O not used)

Legend

STR - TIM = Strain-Time

FRC - DPT = Force-Depth

WRK - DPT = Work-Depth

DPT - TIM = Depth-Time

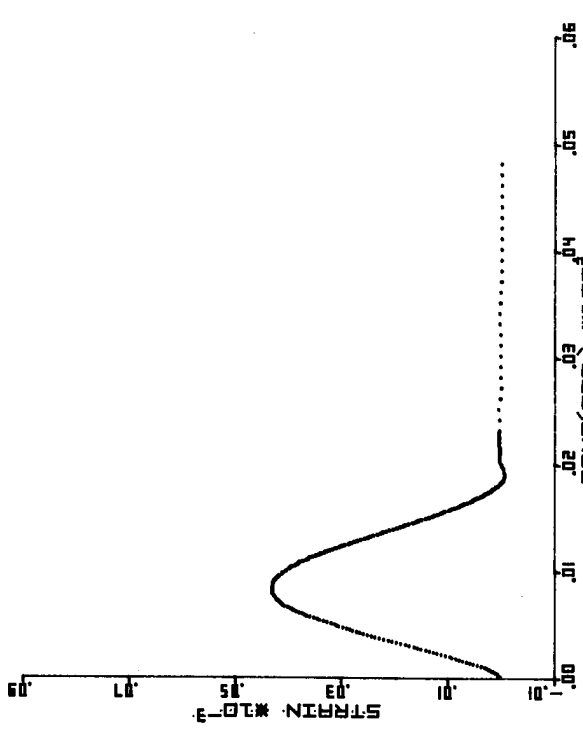


Figure 3.3A-1. PM/19/1.77 STR-TIM

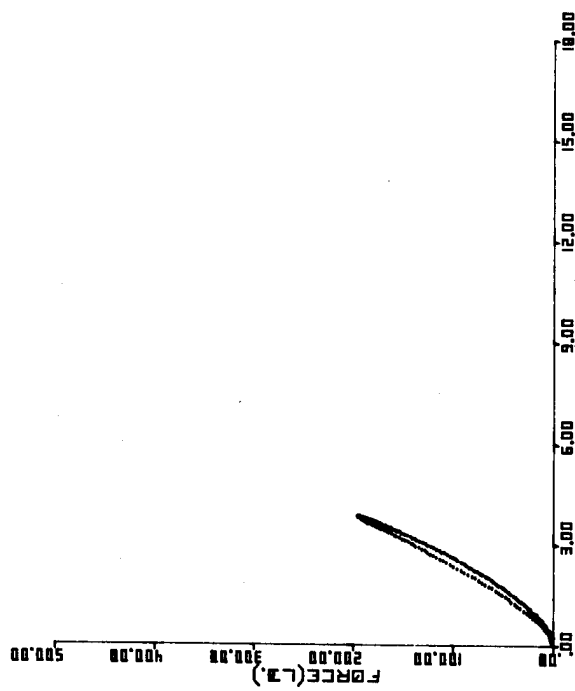


Figure 3.3A-2. PM/19/1.77 FRC-DPT

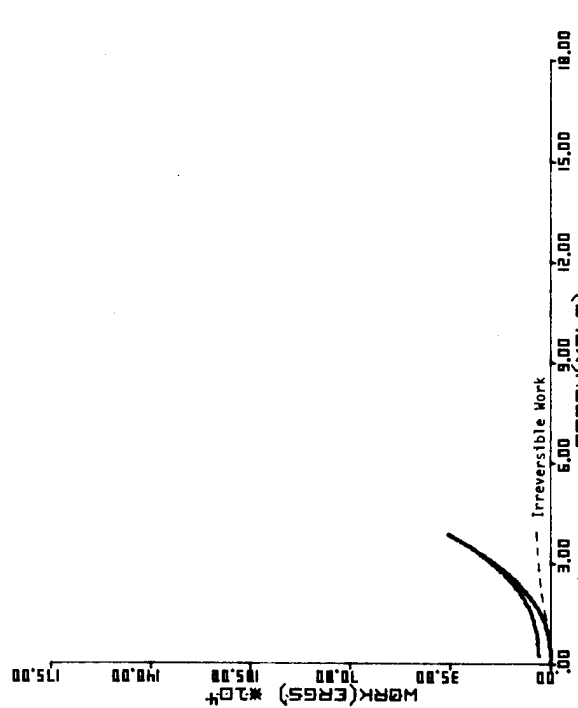


Figure 3.3A-3. PM/19/1.77 WRK-DPT

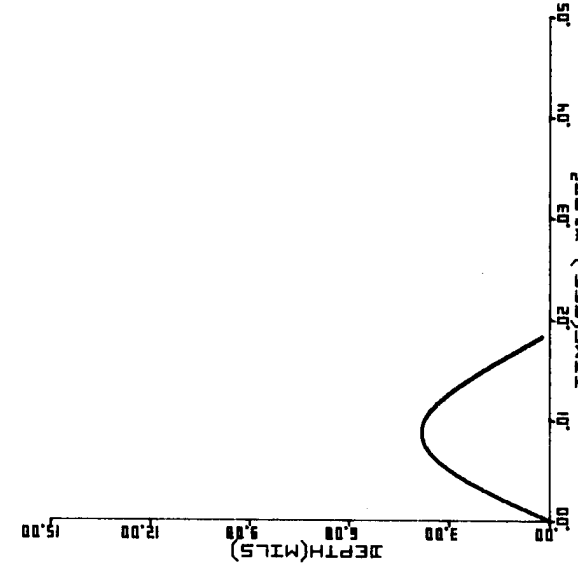


Figure 3.3A-4. PM/19/1.77 DPT-TIM

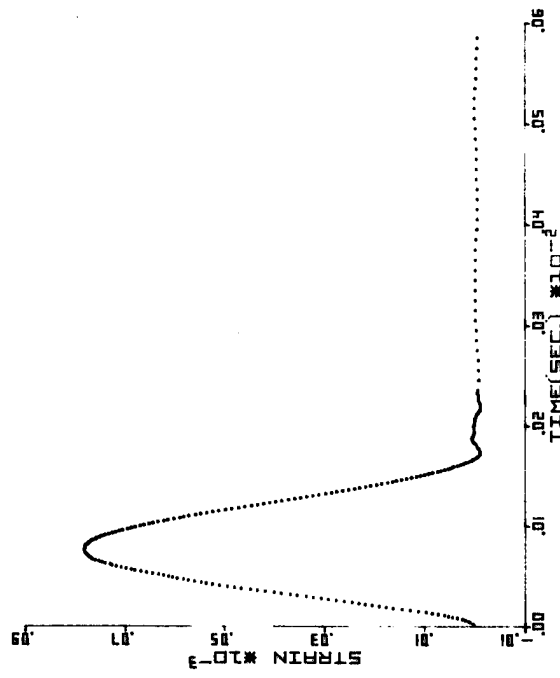


Figure 3.3B-1. PM/19/2.93 STR-TIM

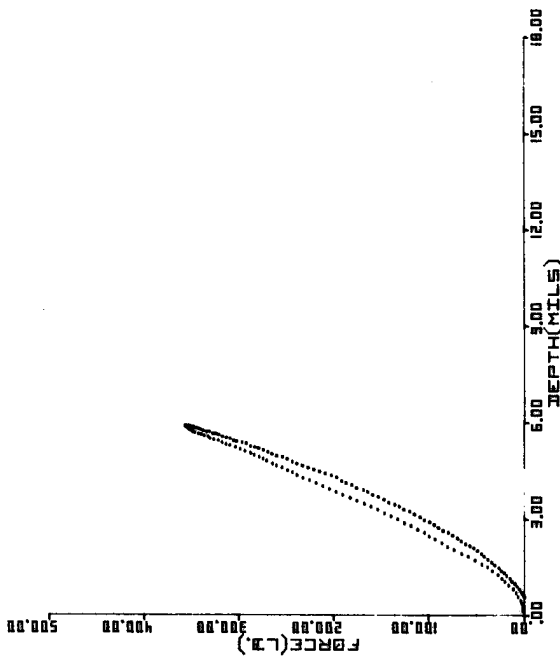


Figure 3.3B-2. PM/19/2.93 FRC-DPT

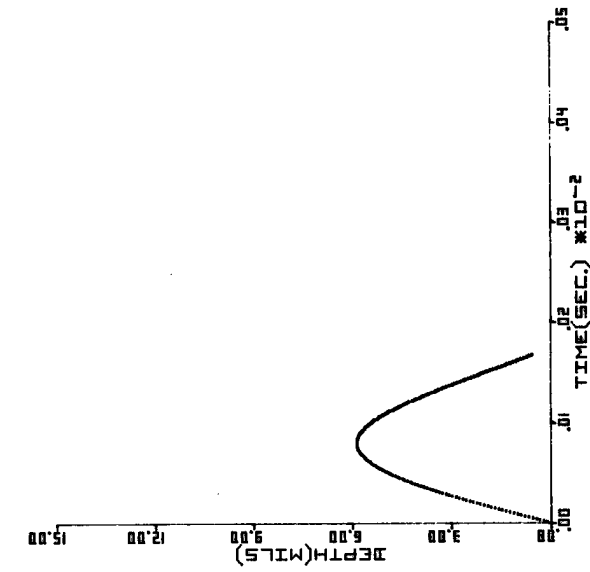


Figure 3.3B-4. PM/19/2.93 DPT-TIM

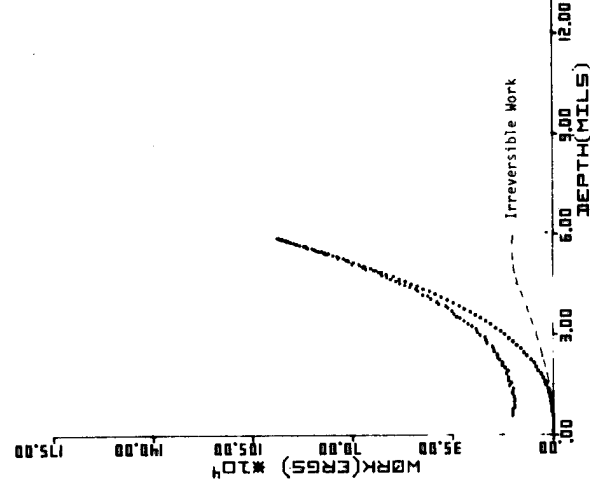


Figure 3.3B-3. PM/19/2.93 WRK-DPT

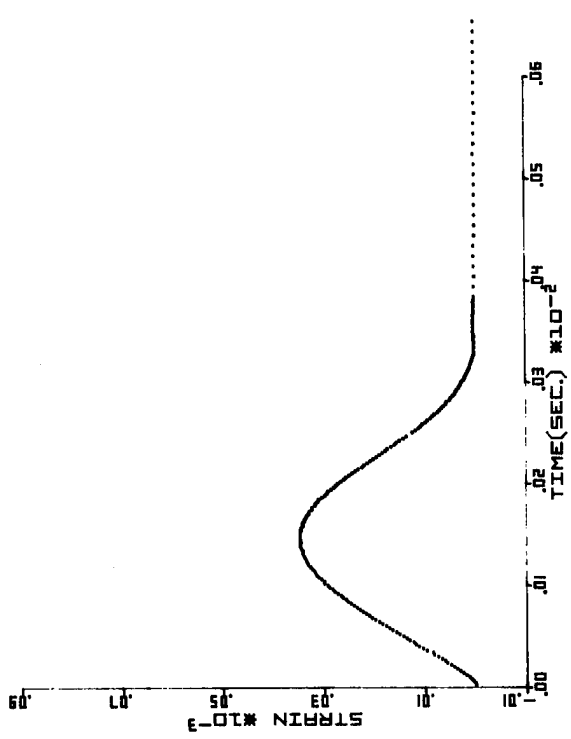


Figure 3.3C-1. PM/4.5/1.77 STR-TIM

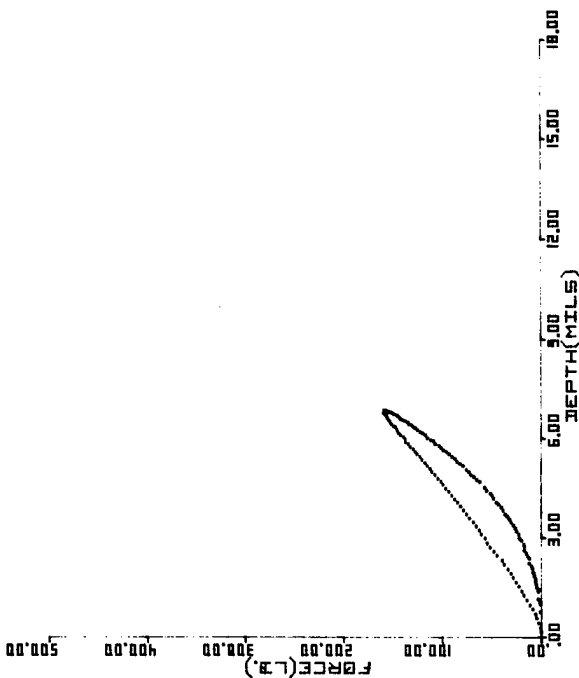


Figure 3.3C-2. PM/4.5/1.77 FRC-DPT

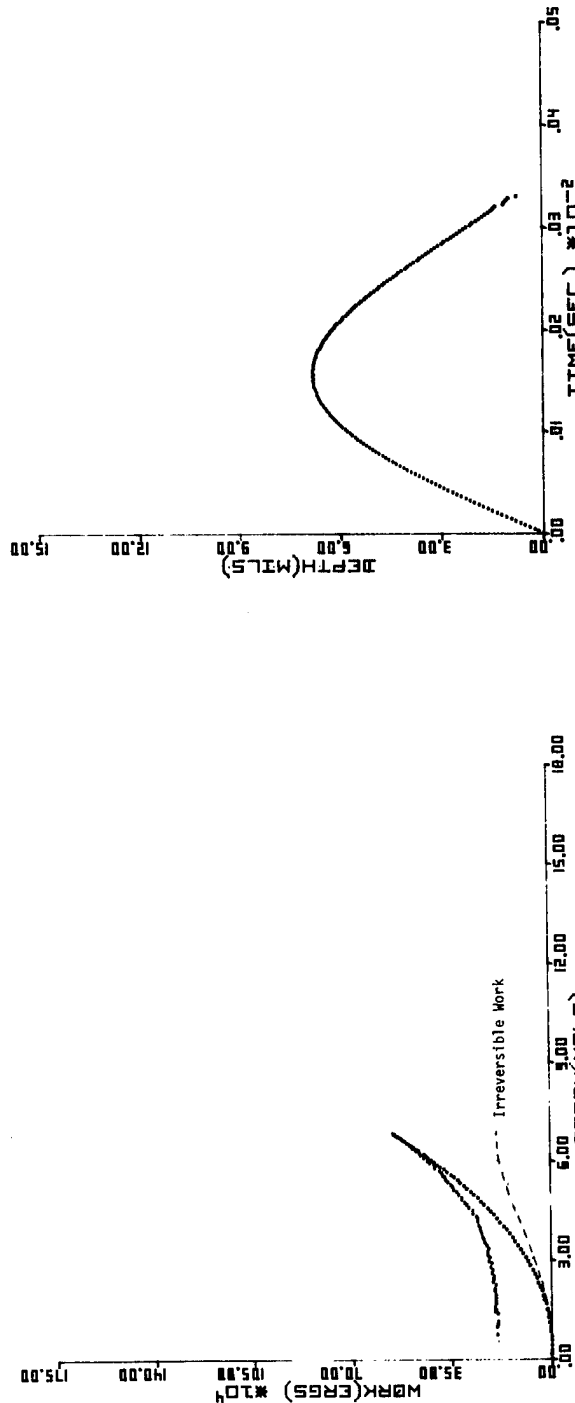


Figure 3.3C-3. PM/4.5/1.77 WRK-DPT

Figure 3.3C-4. PM/4.5/1.77 DPT-TIM

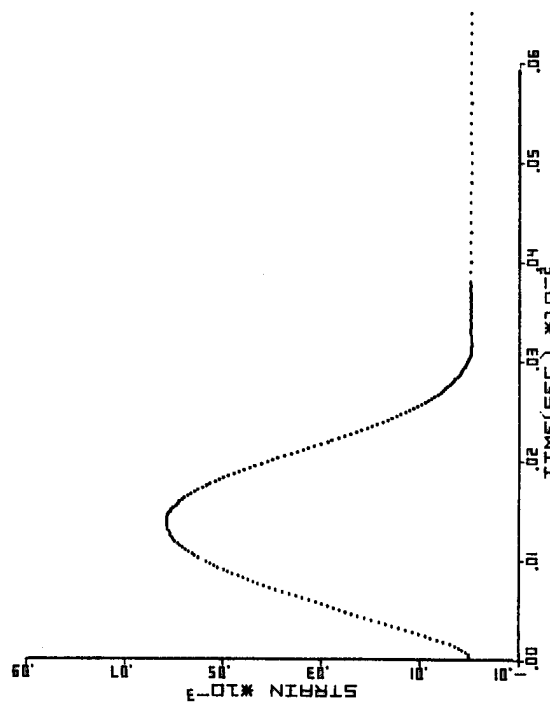


Figure 3.3D-1. PM/4.5/2.92 STR-TIM

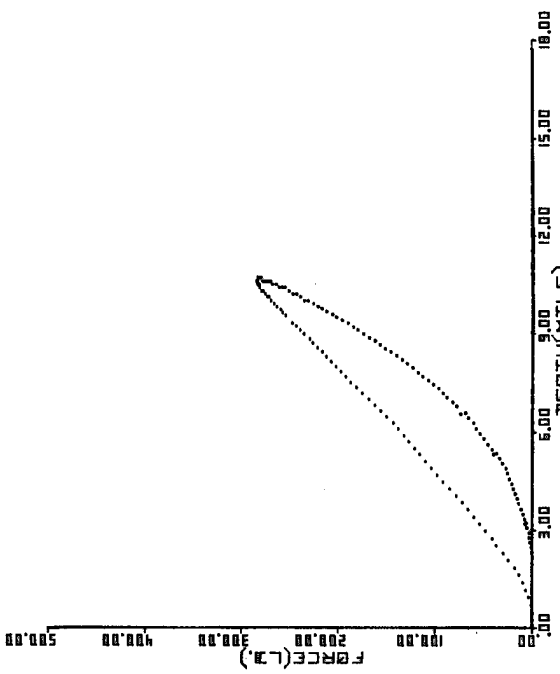


Figure 3.3D-2. PM-4/5/2.92 FRC-DPT

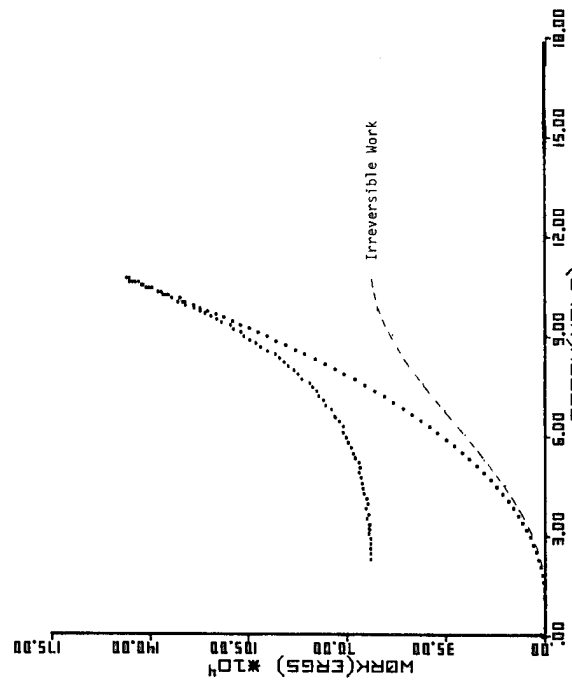


Figure 3.3D-3. PM/4.5/2.92 WRK-DPT



Figure 3.3D-4. PM/4.5/2.92 DPT-TIM

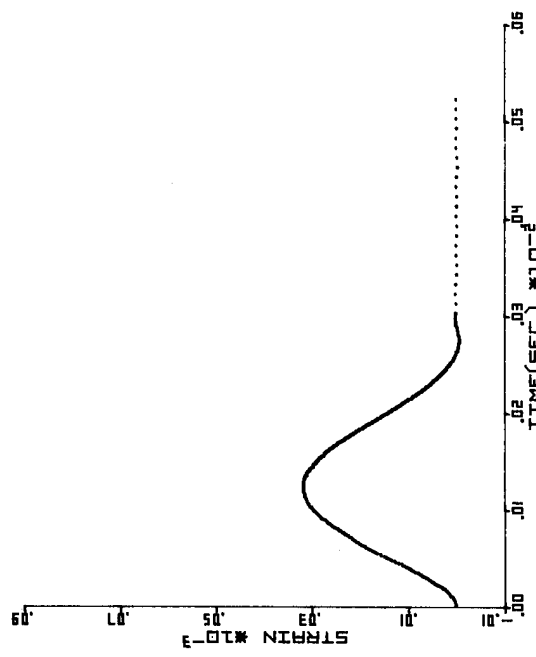


Figure 3.3E-1. PC/19/1.77 STR-TIM

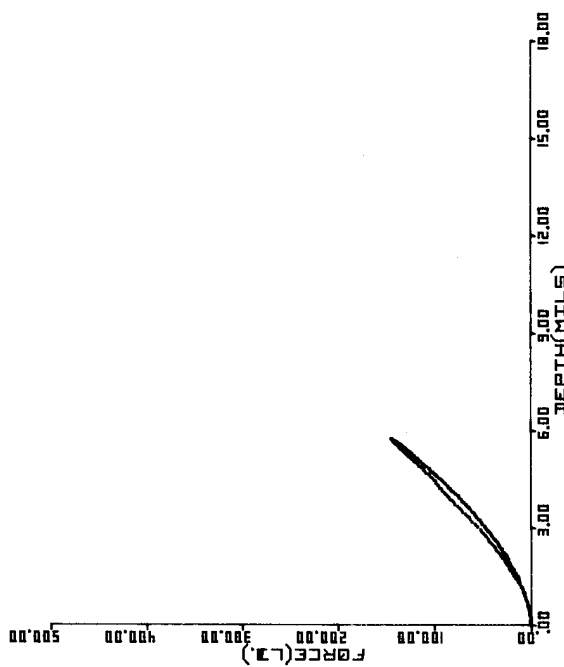


Figure 3.3E-2. PC/19/1.77 FRC-DPT

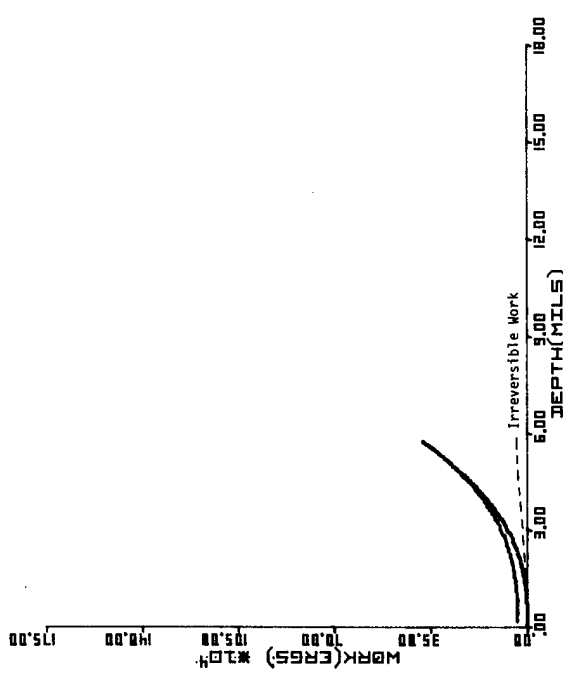


Figure 3.3E-3. PC/19/1.77 WRK-DPT

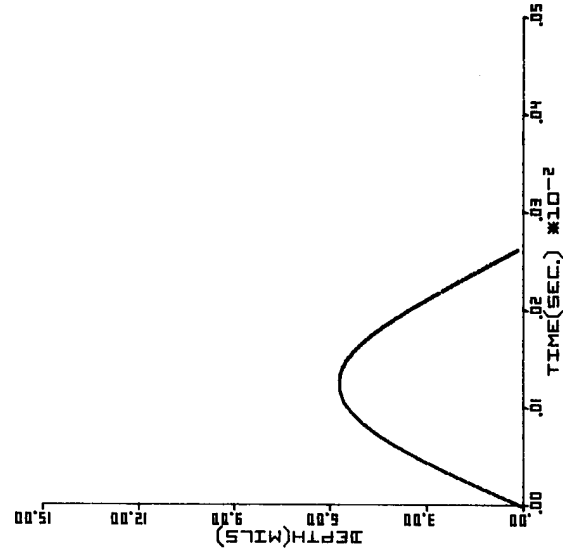


Figure 3.3E-4. PC/19/1.77 DPT-TIM

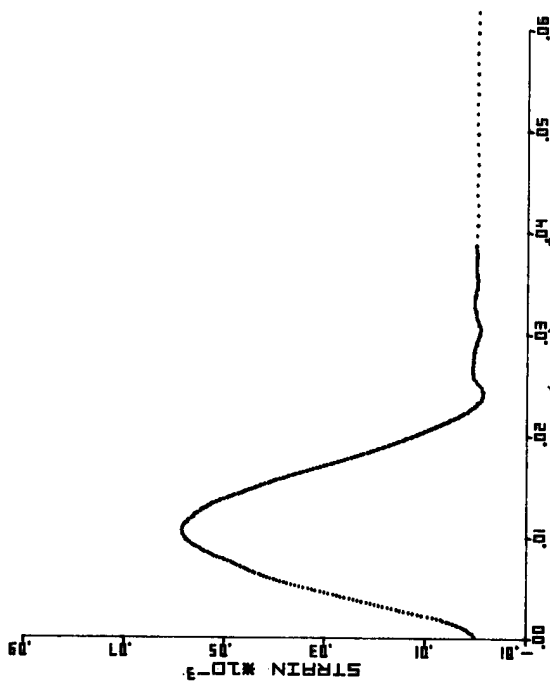


Figure 3.3F-1. PC/19/2.93 STR-TIM

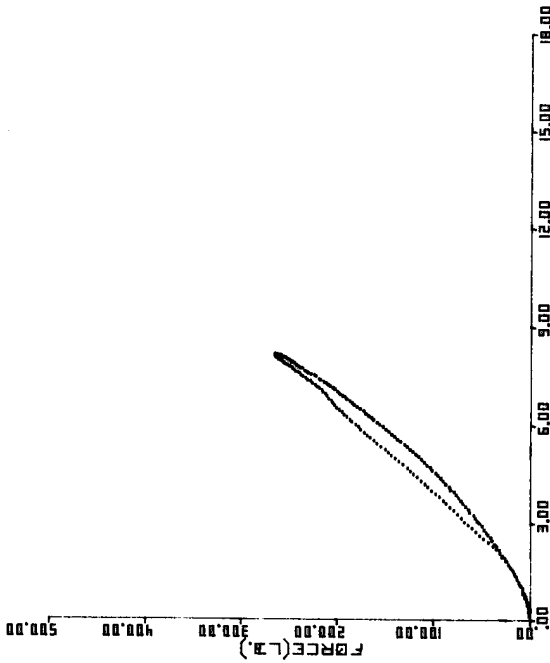


Figure 3.3F-2. PC/19/2.93 FRC-DPT

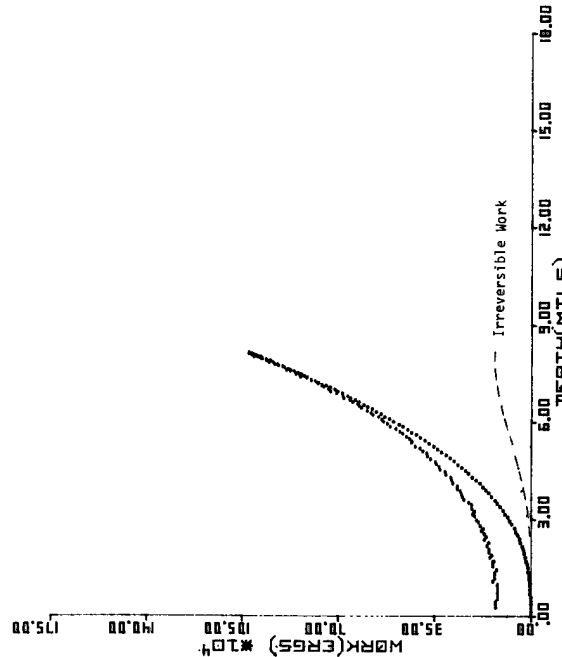


Figure 3.3F-3. PC/19/2.93 WRK-DPT

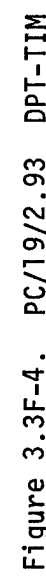


Figure 3.3F-4. PC/19/2.93 DPT-TIM

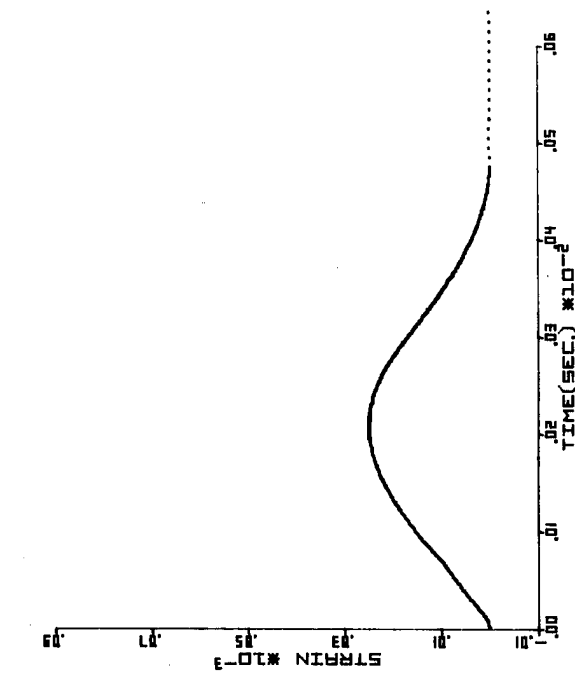


Figure 3.3G-1. PC/4.5/1.77 STR-TIM

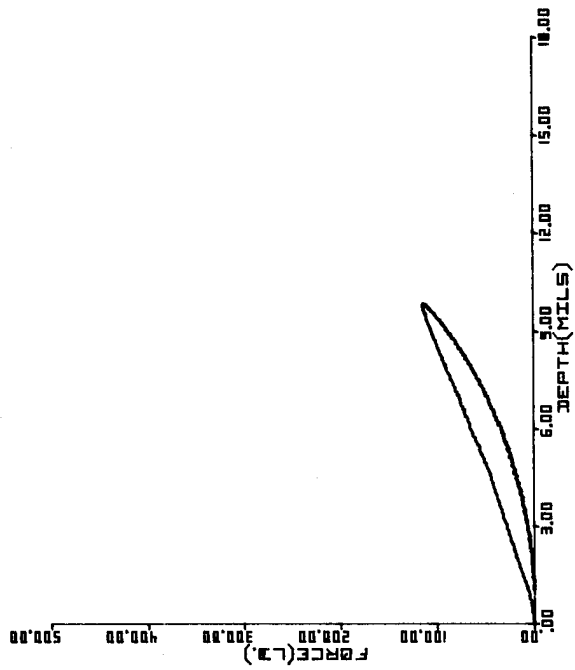


Figure 3.3G-2. PC/4.5/1.77 FRC-DPT

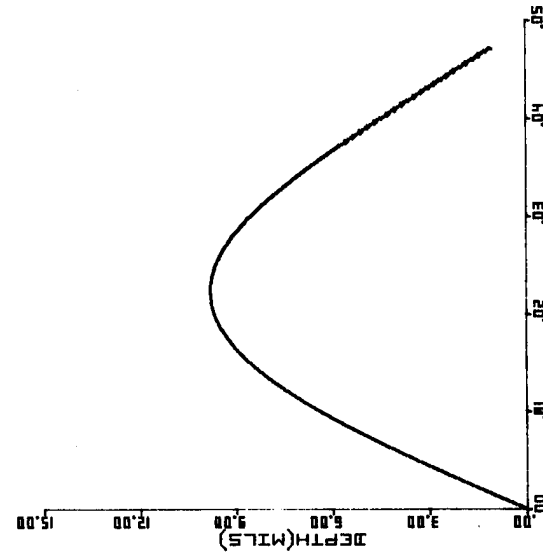


Figure 3.3G-4. PC/4.5/1.77 DPT-TIM

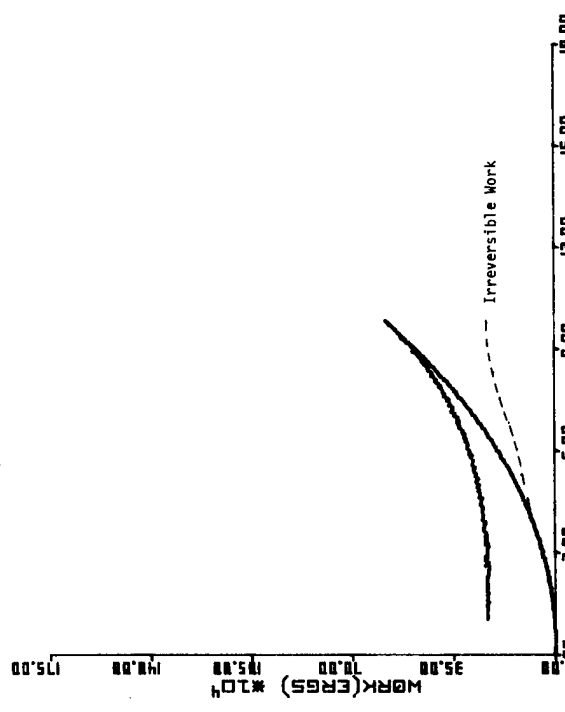


Figure 3.3G-3. PC/4.5/1.77 WRK-DPT

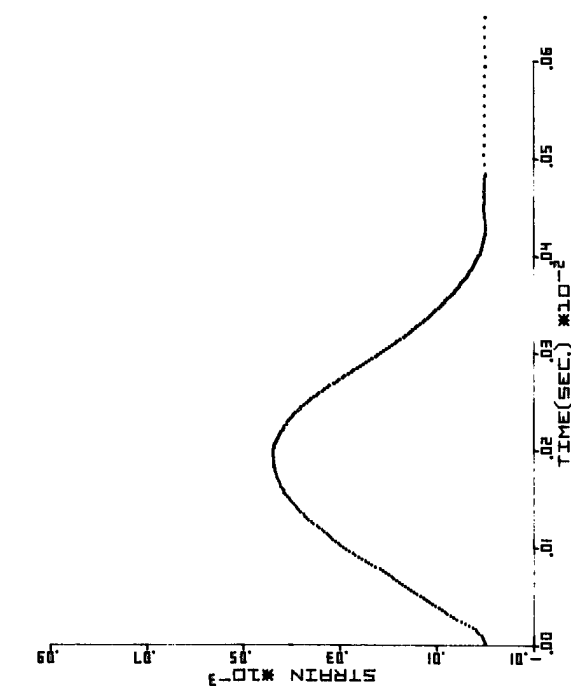


Figure 3.3H-1. PC/4.5/2.90 STR-TIM

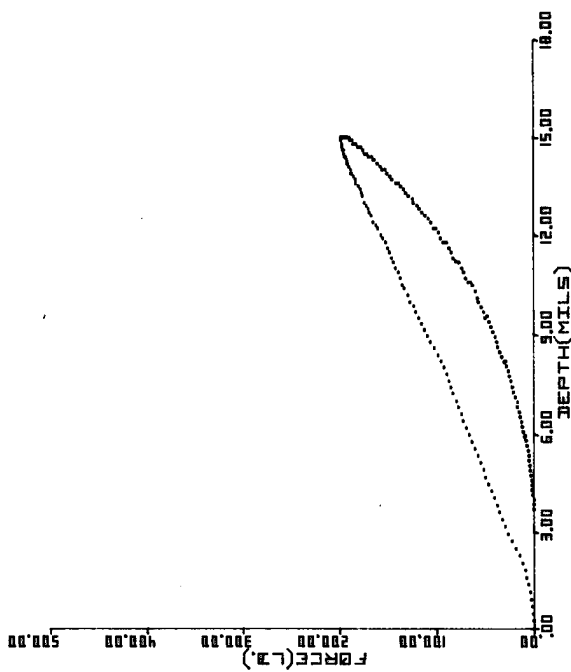


Figure 3.3H-2. PC/4.5/2.90 FRC-DPT

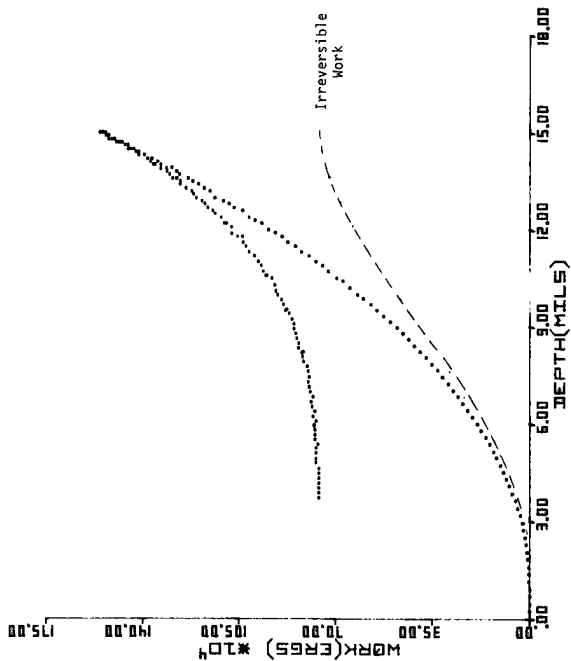


Figure 3.3H-3. PC/4.5/2.90 WRK-DPT

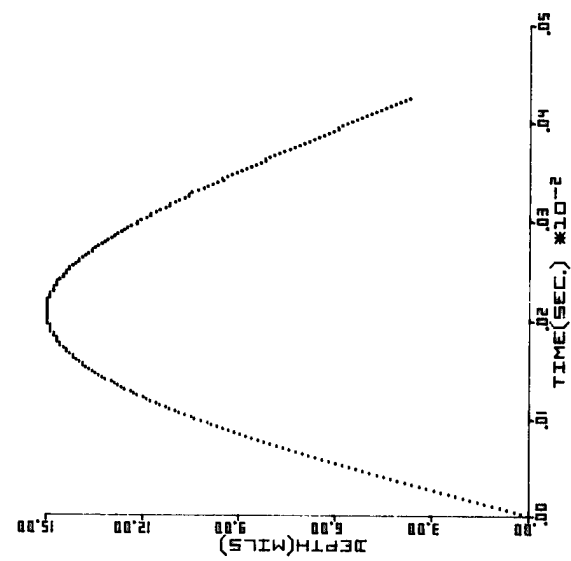


Figure 3.3H-4. PC/4.5/2.90 DPT-TIM

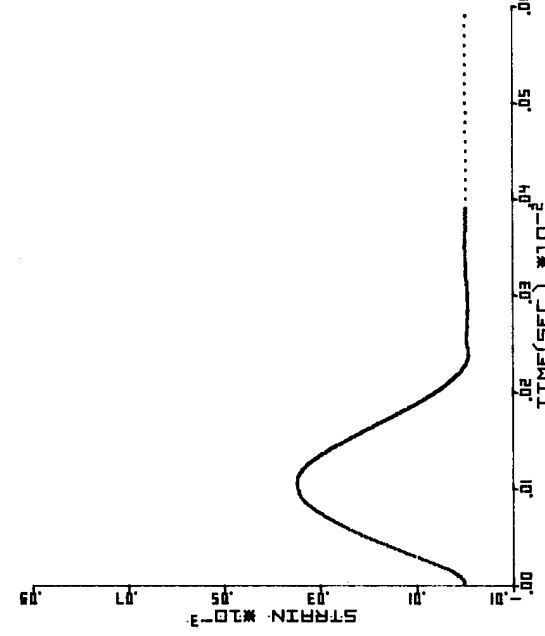


Figure 3.3J-1. EP/19/1.77 STR-TIM

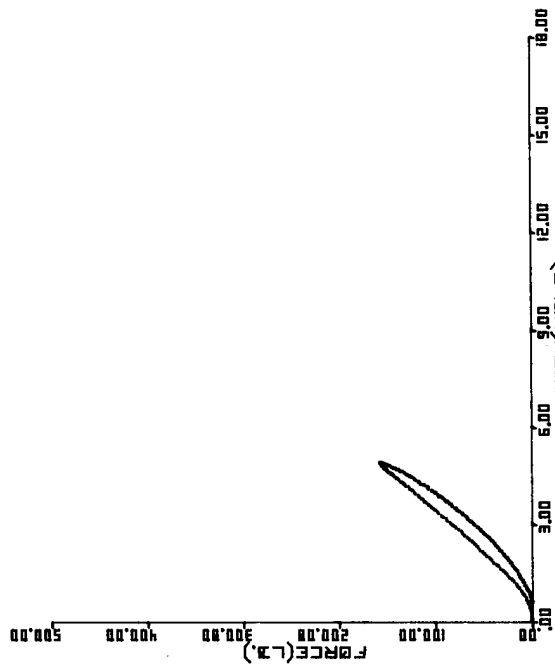


Figure 3.3J-2. EP/19/1.77 FRC-DPT

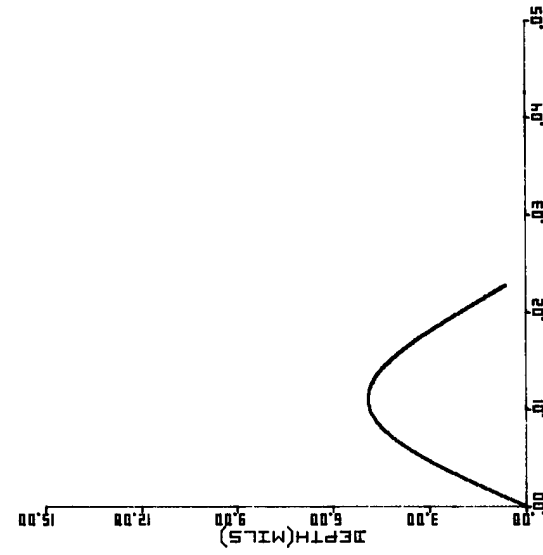


Figure 3.3J-3. EP/19/1.77 WRK-DPT



Figure 3.3J-4. EP/19/1.77 DPT-TIM

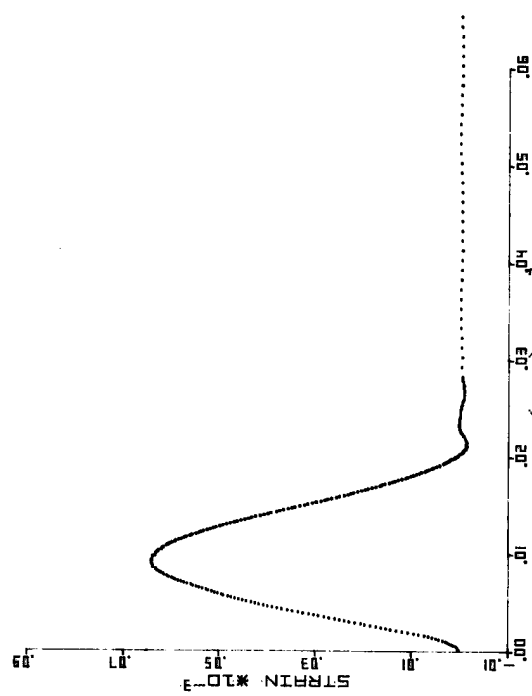


Figure 3.3K-1. EP/19/2.93 STR-TIM

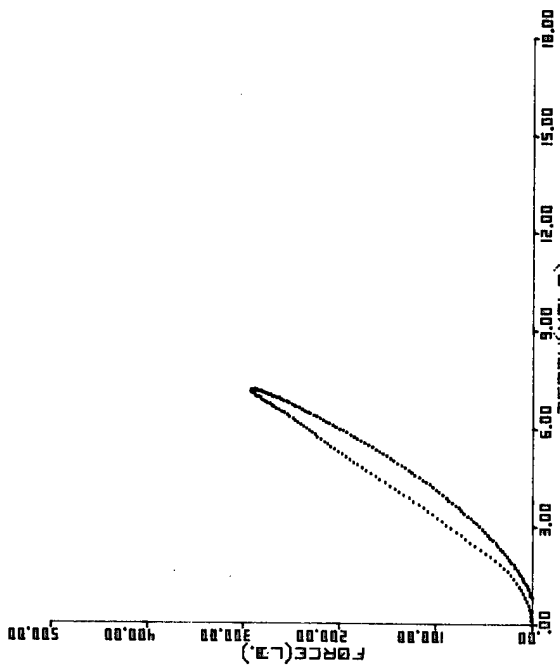


Figure 3.3K-2. EP/19/2.93 FRC-DPT

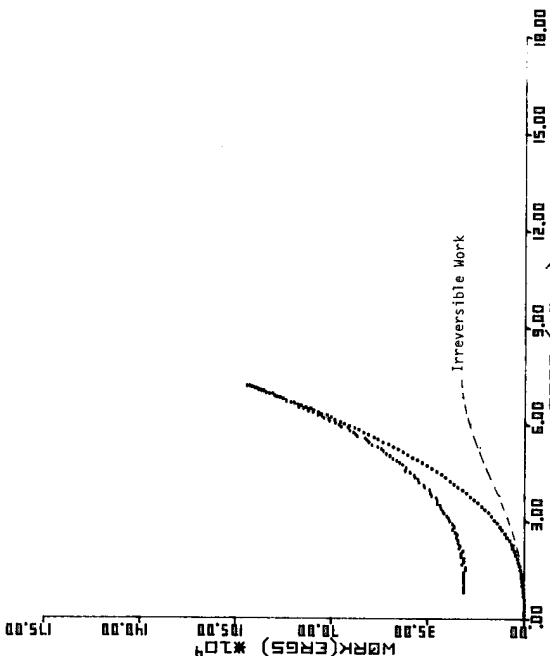


Figure 3.3K-3. EP/19/2.93 WRK-DPT

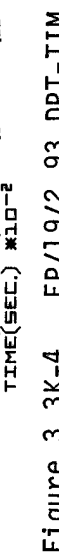


Figure 3.3K-4. EP/19/2.93 DPT-TIM

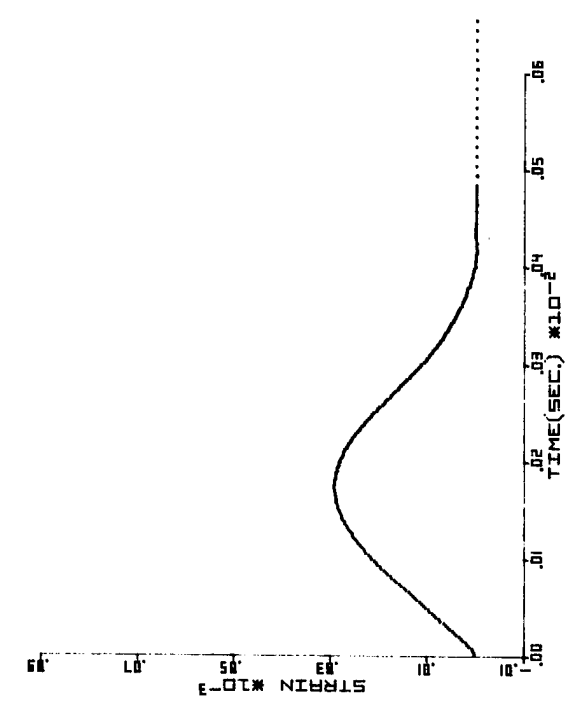


Figure 3.3L-1. EP/4.5/1.77 STR-TIM

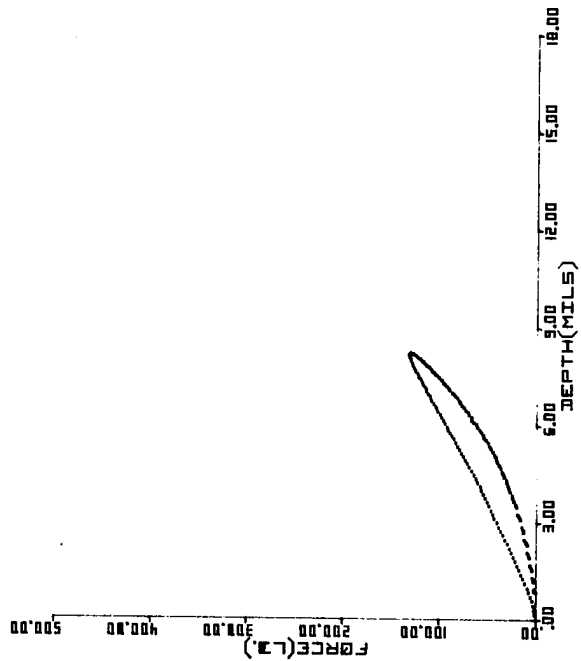


Figure 3.3L-2. EP/4.5/1.77 FRC-DPT

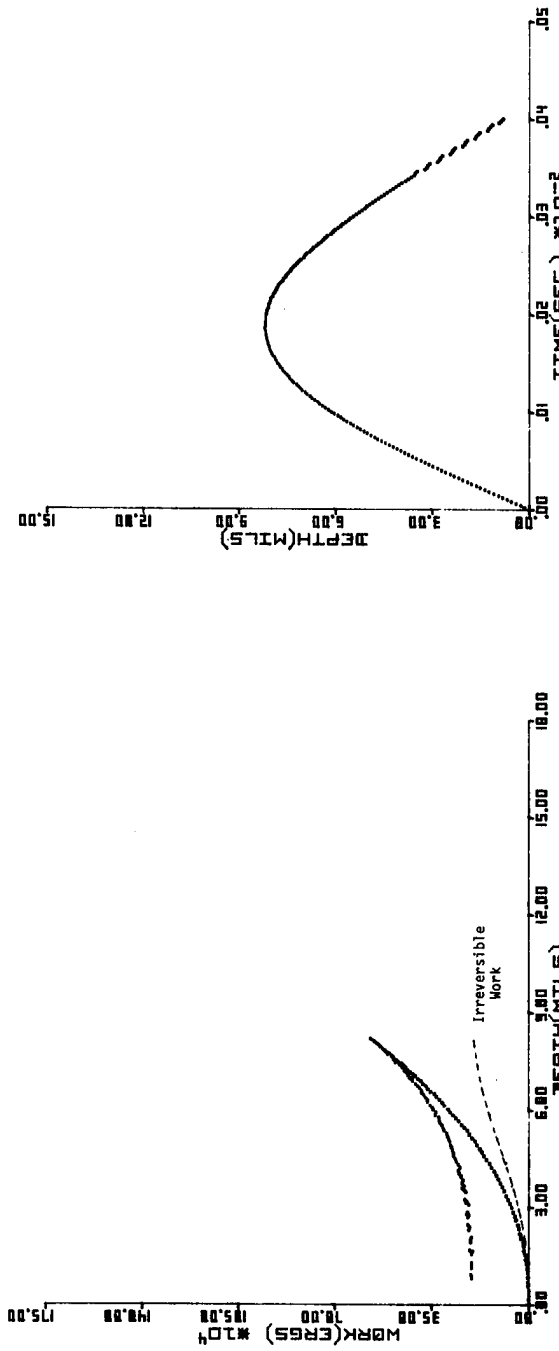


Figure 3.3L-3. EP/4.5/1.77 WRK-DPT

Figure 3.3L-4. EP/4.5/1.77 DPT-TIM

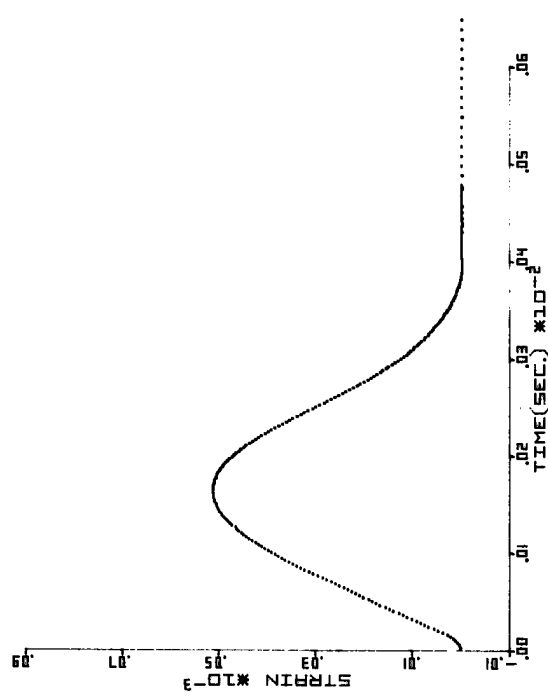


Figure 3.3M-1. EP/4.5/2.92 STR-TIM

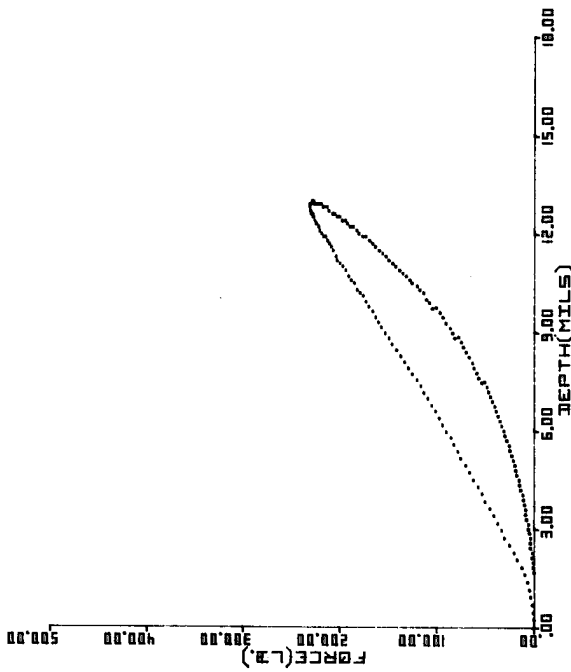


Figure 3.3M-2. EP/4.5/2.92 FRC-DPT

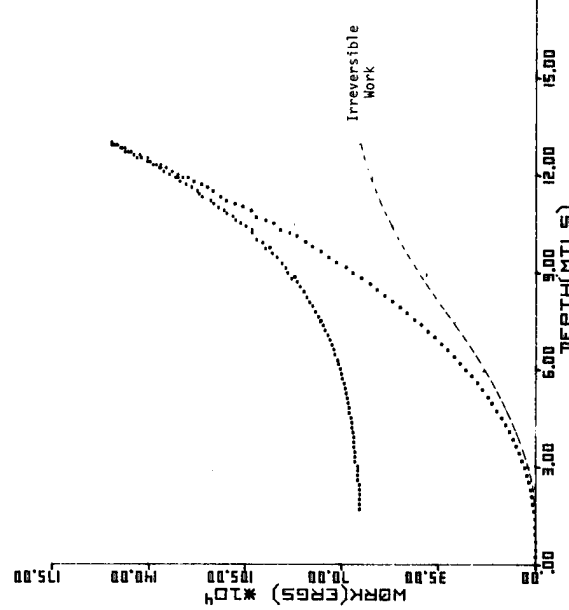


Figure 3.3M-3. EP/4.5/2.92 WRK-DPT

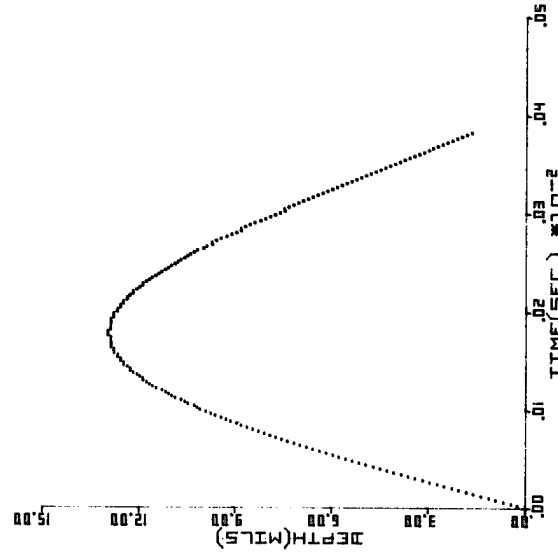


Figure 3.3M-4. EP/4.5/2.92 DPT-TIM

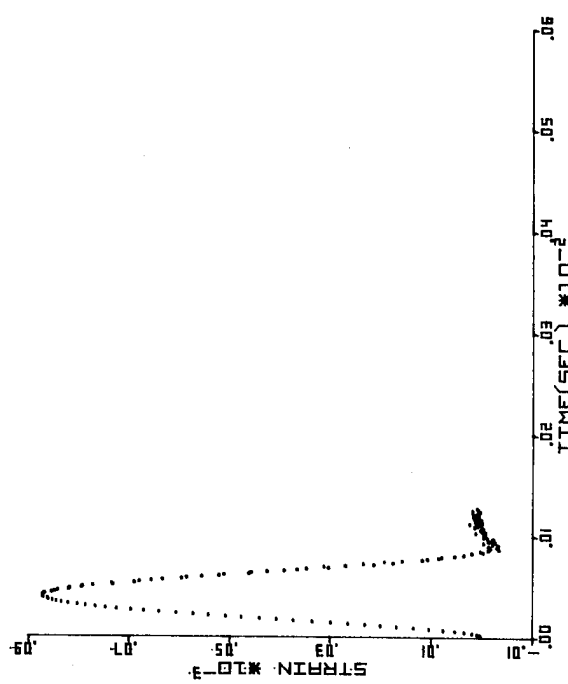


Figure 3.3N-1. G/19/1.77 STR-TIM

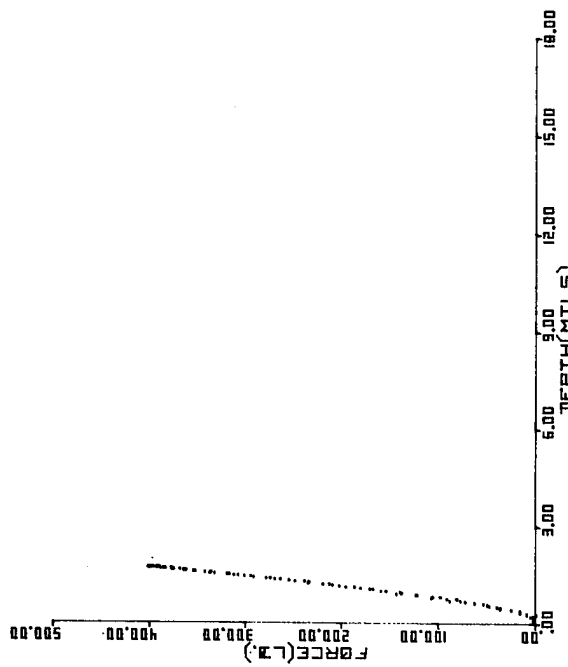


Figure 3.3N-2. G/19/1.77 FRC-DPT

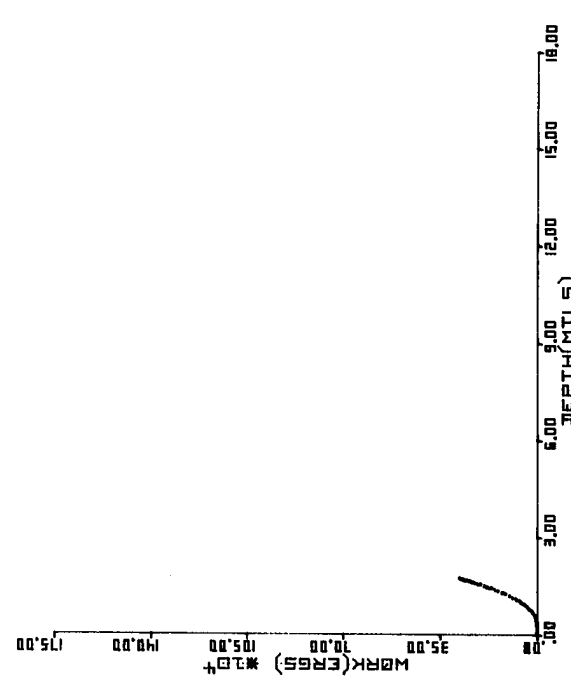


Figure 3.3N-3. G/19/1.77 WRK-DPT

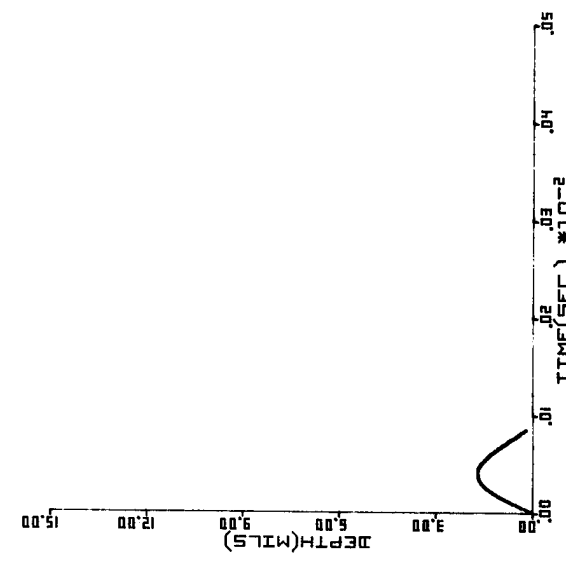


Figure 3.3N-4. G/19/1.77 DPT-TIM

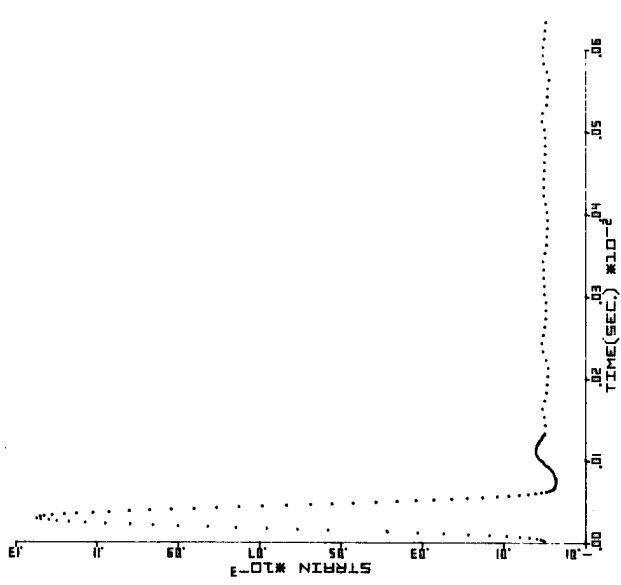


Figure 3.3P-1. SIC/19/1.77 STR-TIM

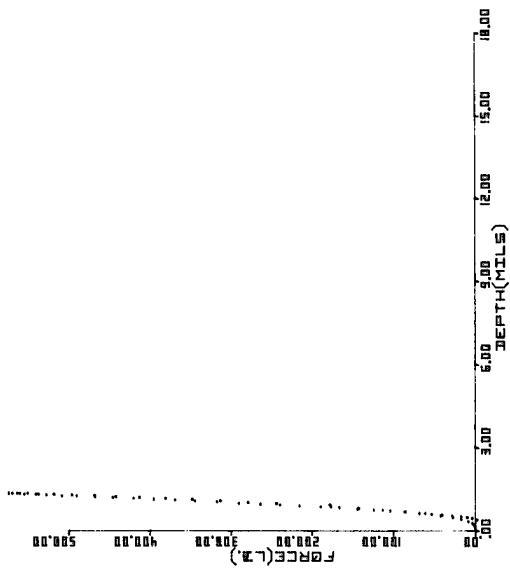


Figure 3.3P-2. SIC/19/1.77 FRC-DPT

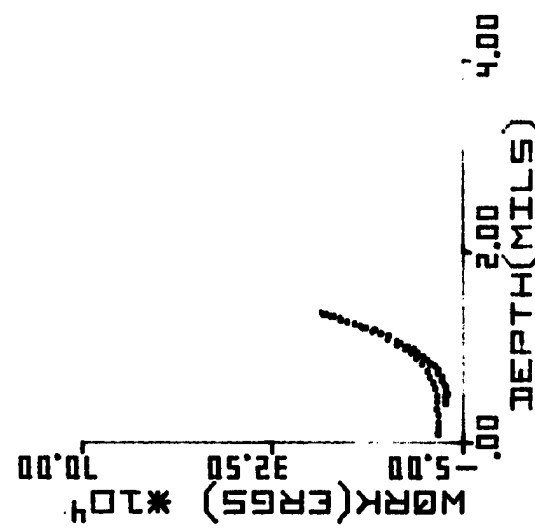


Figure 3.3P-3. SIC/19/1.77 WRK-DPT



Figure 3.3P-4. SIC/19/1.77 DPT-TIM

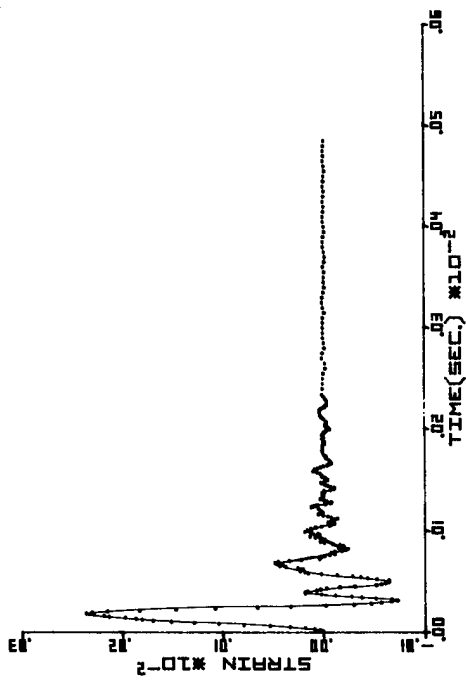


Figure 3.5A-1. PM/4.5/85.4 STR-TIM

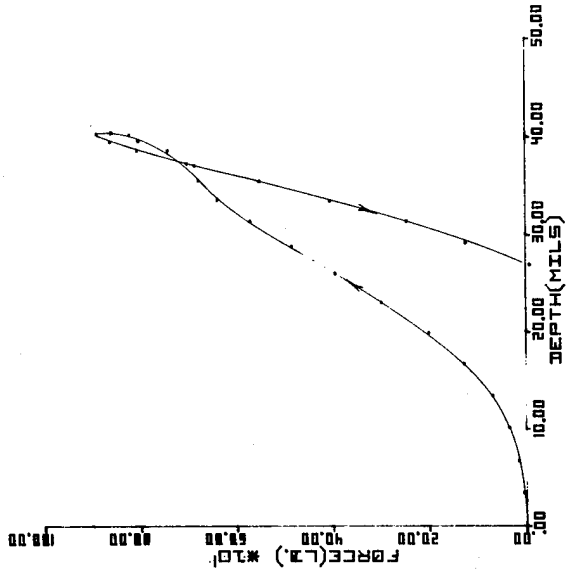


Figure 3.5A-2. PM/4.5/85.4 FRC-DPT

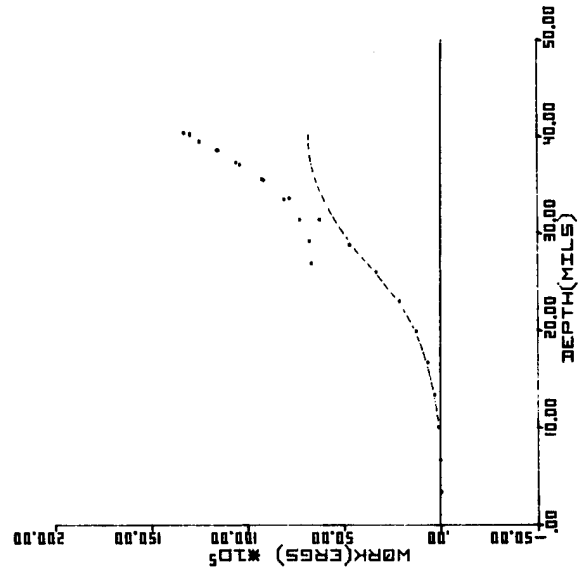


Figure 3.5A-3. PM/4.5/85.4 WRK-DPT

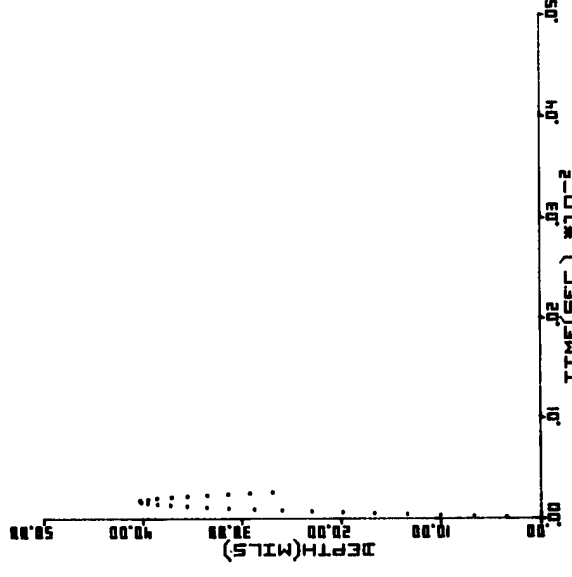


Figure 3.5A-4. PM/4.5/85.4 DPT-TIM

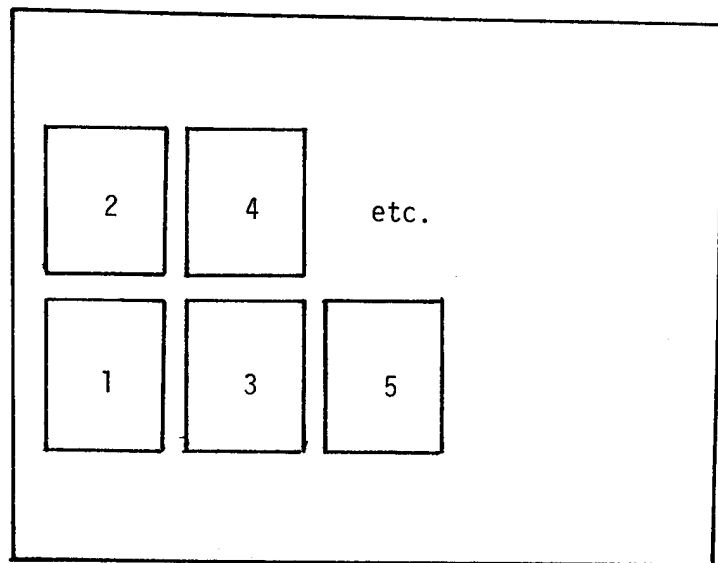


Figure 4.1A. Ima-Con Framing Sequence

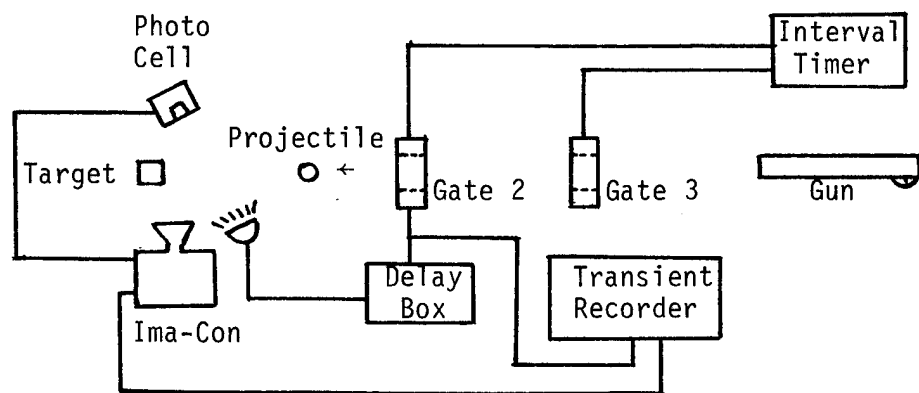


Figure 4.1B. Schematic Diagram of the Triggering/Monitoring Circuit

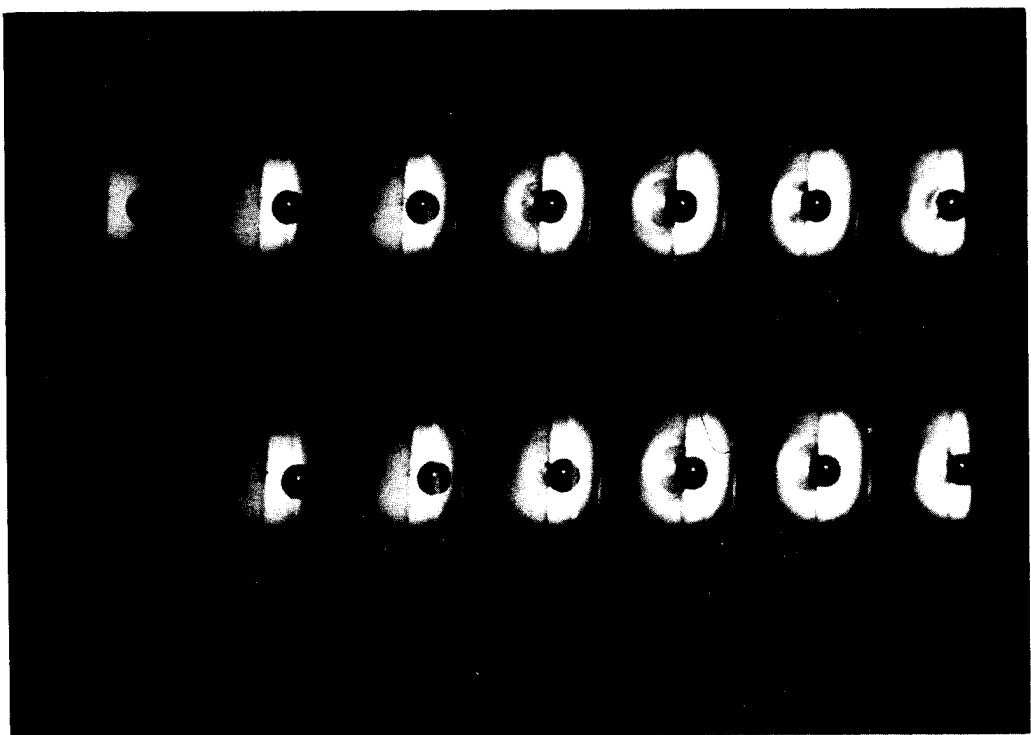


Figure 4.2A. Impact of a 4.5 mm Steel Ball,  $v_i = 140.5$  m/sec., on PC.  
Approximately 5  $\mu$ s/frame.

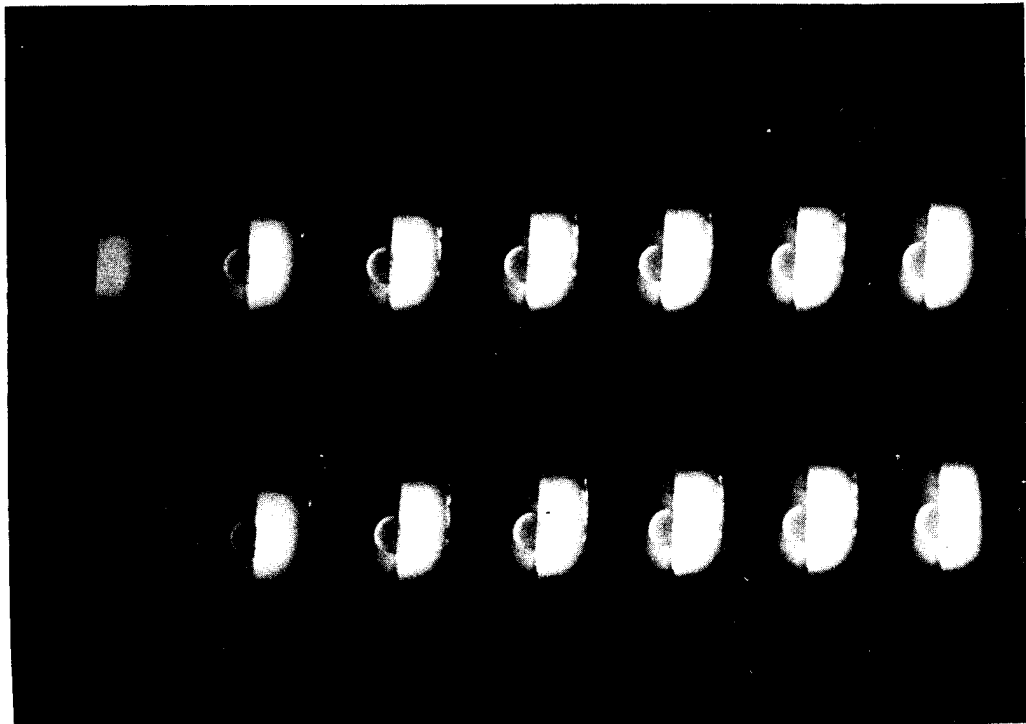
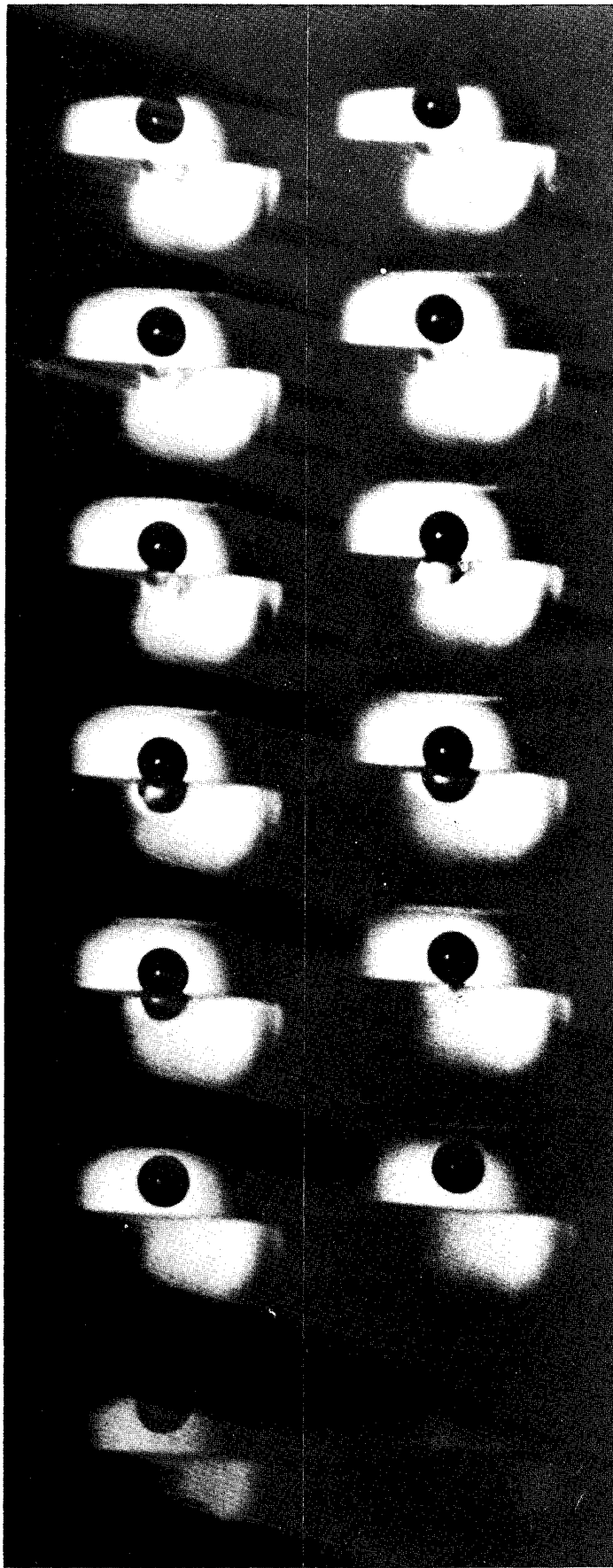


Figure 4.2B. PC Sample from Figure 4.2A Rephotographed Several Minutes  
After Impact



F-26

1st Appearance of Crack, Frame 9  
Max. Extent of Crack, Frames 10-14  
Densified Zone at Max. Penetration  
Frame 8

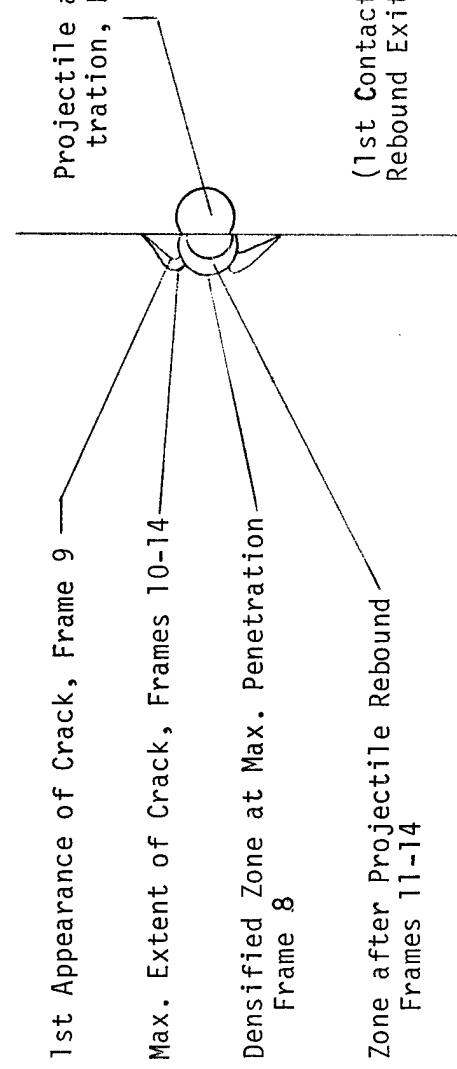


Fig. 4.2C. Impact of 4.5 mm steel ball,  $v_i = 140.5$  m/sec, on PMMA.  
Approximately 5  $\mu$ s/frame.

Composite Schematic of Impact Sequences

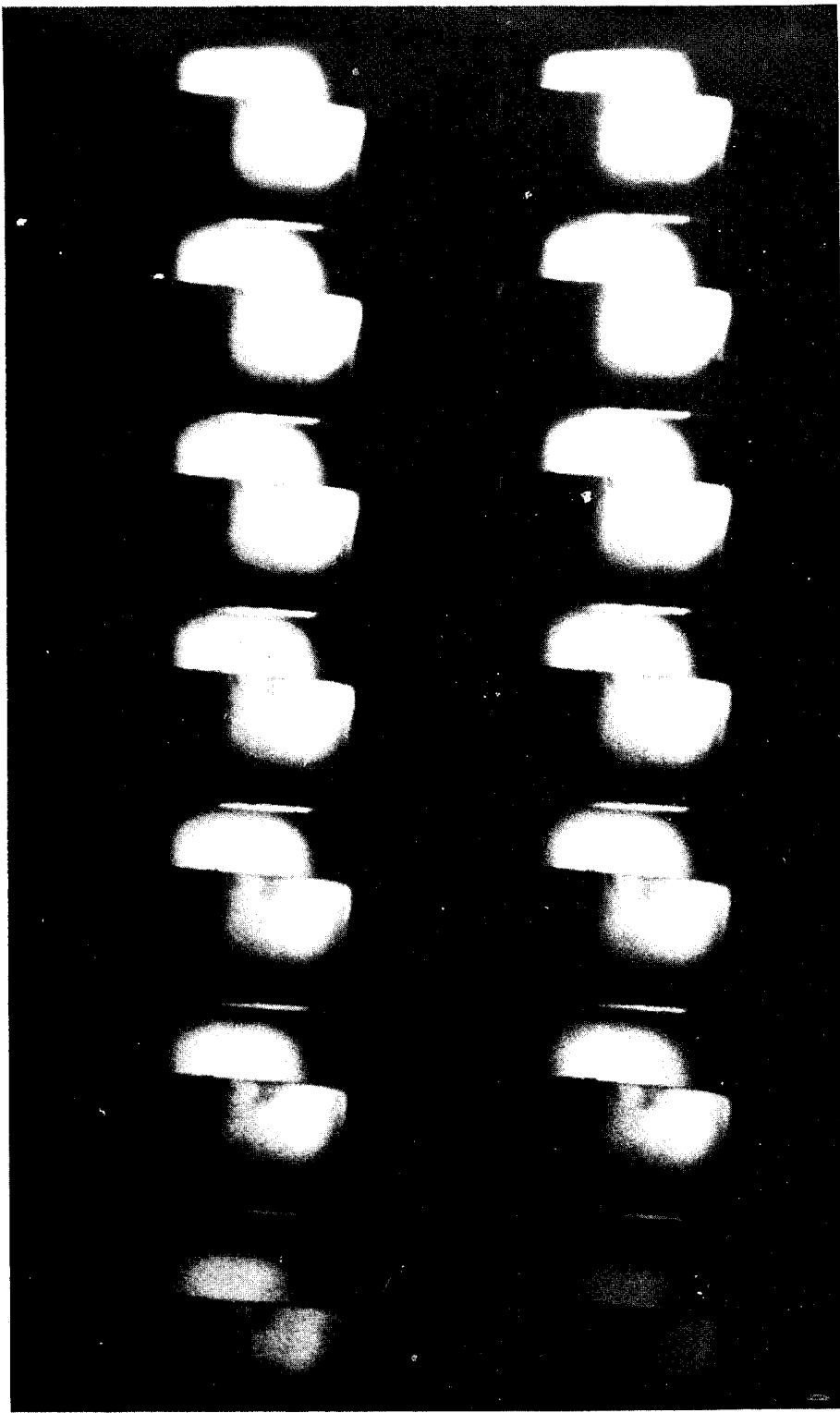


Figure 4.2D. PMMA Sample from Figure 4.2C Rephotographed Several Minutes After Impact

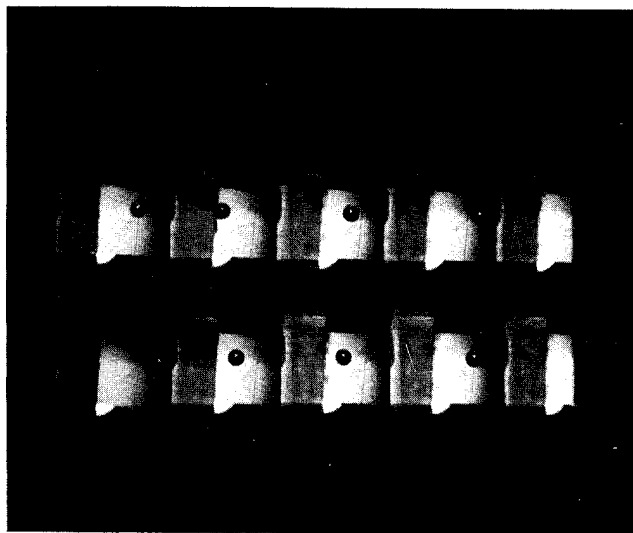


Figure 4.2E. Impact of 4.5 mm Steel Ball,  $v_i$  = 142.4 m/sec, on PMMA. Approximately 40  $\mu$ s/frame.

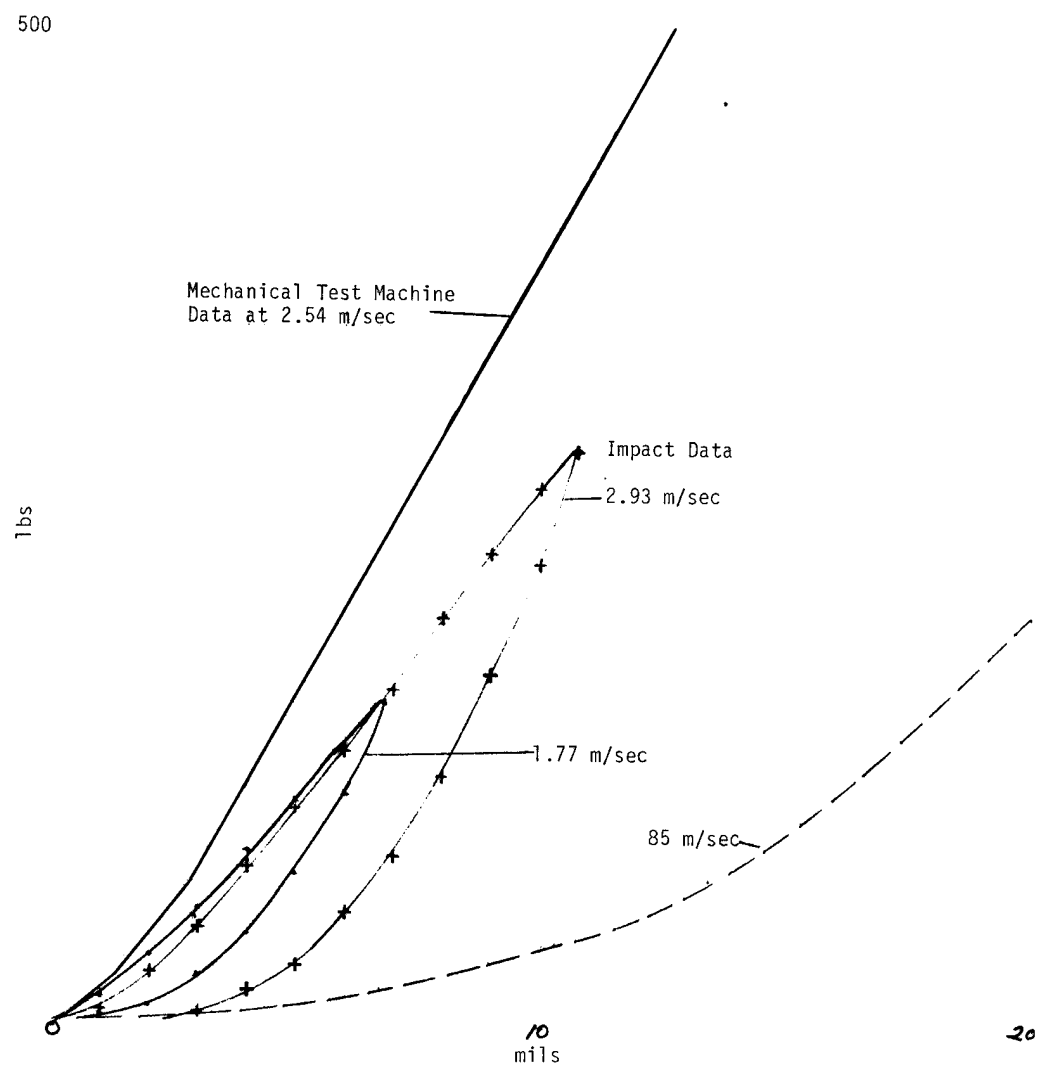


Figure 5A. Force-Penetration Response of PMMA Using 4.5 mm Striker

## APPENDIX

### Summary of Impact Pulse Computational Procedures

#### Primary Data

$m_s$  = mass of striker  
 $m_b$  = mass of impact bar  
 $h_i$  = starting height of striker before swing  
 $h_o$  = minimum height of striker at point of impact  
 $h_f$  = final maximum height of striker on rebound  
 $L$  = amplitude of swing of impact bar  
 $\epsilon$  = strain as recorded on digital storage oscilloscope  
 $A$  = cross-sectional area of impact bar  
 $E$  = Young's modulus of impact bar  
 $c$  = velocity of sound in impact bar  
 $g$  = gravitational constant  
 $R$  = length of supporting filament corresponding to a pendulum length  
 $t$  = time interval since initial striker contact

#### Computed Quantities

$v_o$  = impact velocity of striker =  $\sqrt{2g(h_i - h_o)}$   
 $v_f$  = rebound velocity of striker =  $\sqrt{2g(h_f - h_o)}$   
 $p_s$  = momentum transferred from striker =  $m_s|v_o| + m_s|v_f|$

Computed Quantities - con'd.

$v_b$       velocity imparted to bar =  $L\sqrt{g/R}$

$m_b$  = momentum      "      "      " =  $m_b v_b$

$\beta$  = calibration factor =  $p_s / (AE \int_0^\infty \epsilon dt)$

$F$  = force exerted on impact bar =  $AE\beta\epsilon$

$\dot{z}$  = velocity of striker during impact =  $v_0 - \frac{AE\beta}{m_s} \int_0^t \epsilon dt$

$z$  = travel of striker =  $\int_0^t \dot{z} dt$

$w$  = elastic shortening of impact bar =  $c \int_0^t \epsilon dt$

$x$  = penetration of striker into target =  $z - w$

$\dot{x}$  = penetration velocity =  $\dot{z} - c\epsilon$

$U$  = energy extracted from striker =  $\frac{1}{2} m_s (v_0^2 - \dot{z}^2)$

$X$  = energy contained in traveling strain pulse =  $AEc \int_0^t \epsilon^2 dt$

$W$  = local energy in specimen =  $U - X$

## DISTRIBUTION LIST

Contract No. N00019-77-C-0441

Naval Air Systems Command Attn: Code AIR-52032 Washington, DC 20361	14	Air Force Materials Laboratory Wright-Patterson Air Force Base Dayton, OH 45433 Attn: LN 1 LAE 1 LNC 1 MX 1 LNE 1 LY 1 LNP 1 LT 1 MBC 1 (T. J. Reinhart)	9
Naval Air Systems Command Attn: Code AIR-604 Washington, DC 20361	12		
Office of Naval Research Washington, DC 20361 Attn: Code 471 Code 472 Code 473	3	Naval Research Laboratory Washington, DC 20390 Attn: Code 6000 Code 6100 Code 8433	3
Naval Ordnance Laboratory White Oak, MD 20910 Attn: Code 2301 Code 234	2	US Department of Energy Technical Information Service P.O. Box 62 Oak Ridge, TN 37830	1
Materials Sciences & Engineering Laboratory Stanford Research Institute Menlo Park, CA 94025	1	NASA Headquarters Attn: B. G. Achhammer Washington, DC 20546	1
Institute for Materials Research National Bureau of Standards Washington, DC 20234	3	NASA-Lewis Research Center Attn: R. F. Lark, Mail Stop 49-1 21000 Brookpark Road Cleveland, OH 44135	1
Battelle Memorial Institute 505 King Avenue Columbus, OH 43201	1	Army Materials & Mechanics Research Center Watertown, MA 02172 Attn: Dr. R. N. Katz Dr. G. Thomas Dr. R. Lewis Materials Science Lab.	3
IIT Research Institute Attn: Ceramics Division 10 West 35th Street Chicago, IL 60616	1	U. S. Army Aviation Material Laboratories Fort Eustis, VA 23604	1
Naval Ship R&D Center Washington, DC 20007	1	Effects Technology, Inc. Attn: F. R. Tuler P.O. Box 30400 Santa Barbara, CA 93105	1
Naval Ship R&D Center Annapolis Lab. (Code 287) Annapolis, MD 21402			

Naval Undersea R&D Center San Diego, CA 92117	1	Plastics Technical Evaluation Center Picatinny Arsenal Dover, NY 07801	1
Engineering Experiment Station Georgia Institute of Technology Atlanta, GA 30332		University of Dayton Library on Materials Research	1
Goodyear Aerospace Corporation Attn: G. Wintermute Litchfield Park, AZ 85340	1	300 College Park Avenue Dayton, OH 45409	
Pratt & Whitney Aircraft Div. United Aircraft Corporation Attn: C. C. Goodrich East Hartford, CT 06108	1	University of Michigan Attn: F. G. Hammitt Dept. of Nuclear Engineering Ann Arbor, MI 48104	1
TRW Equipment Lab 23555 Euclid Avenue Cleveland, OH 44117	1	Olin Corporation Chemical Group New Haven, CT 06540	1
Aero-Electronic Technology Dept. Attn: George Tatnall Naval Air Development Center Warminster, PA 18974	1	Aerospace Corporation Materials Laboratory P.O. Box 95085 Los Angeles, CA 90045	1
Vought Aeronautics Division Attn: A. E. Hohman, Jr. LTV Aerospace Corporation P.O. Box 5907 Dallas, TX 75222	1	Air Force Avionics Laboratory Wright Patterson AFB Dayton, OH 45433 Attn: AVTL	1
Engineered Fabrics Division Goodyear Aerospace Corporation Akron, OH 44315	1	U.S. Army Research Office Box CM, Duke Station Durham, NC 27706	1
Bell Aerosystems Company Attn: N. E. Wahl Buffalo, NY 14240	1	Applied Technology Division Avco Corporation Lowell Industrial Park Lowell, MA 01851	1
Hydronautics, Incorporated Pindell School Road Howard County Laurel, MD 20810	1	Solar Division Attn: Dr. A. G. Metcalfe International Harvester Company 2200 Pacific Highway San Diego, CA 92112	1
Brunswick Corporation Marion, VA 24354	1	Material Sciences Corporation 17777 Walton Road Blue Bell, PA 19422	1

University of Illinois 1  
 Attn: Prof. H. T. Corten  
 Dept. of Theoretical & Applied  
 Mechs.  
 Urbana, IL 61801

Naval Ship Engineering Center 1  
 Attn: Code 6101E  
 Washington, DC 20361

Westinghouse Research Labs. 1  
 Attn: R. Bratton  
 Beulah Road  
 Pittsburgh, PA 15235

E. I. duPont deNemours & Company 1  
 Attn: C. Zweben, Bldg. 262  
 Textile Fibers Dept.  
 Carothers Research Lab  
 Experimental Station  
 Wilmington, DE 19898

NTDSC 1  
 Southwest Research Institute  
 P.O. Drawer 28510  
 San Antonio, TX 78284

Texas A&M University 1  
 Attn: Prof. J. L. Rand  
 Aerospace Engineering Dept.  
 College Station, TX 77843

Dr. George C. Chang 1  
 Advanced Physical Methods Branch  
 Division of Energy Storage Systems  
 Office of Conservation  
 US Department of Energy  
 Washington, DC 20545

Prof. D. Uhlmann 1  
 Massachusetts Institute of  
 Technology  
 Cambridge, MA 02139

1 Dr. S. S. Sternstein  
 Rensselaer Polytechnic Institute  
 110 8th Street  
 Troy, NY 12181

1 Prof. R. Doremus  
 Rensselaer Polytechnic Institute  
 110 8th Street  
 Troy, NY 12181

1 Prof. M. Goldstein  
 Belfer Graduate School  
 Yeshiva University  
 500 W. 185 Street  
 New York, NY 10033

John D. Ferry 1  
 Department of Chemistry  
 University of Wisconsin  
 Madison, WI 53706

Library 1  
 1 National Bureau of Standards  
 Washington, DC 20234

Prof. J. H. Gibbs 1  
 Metcalf Chem. Lab.  
 1 Brown University  
 Providence, RI 02912

Polymer Research Institute 1  
 Univ. of Massachusetts  
 1 Amherst, MA 01002

Dr. T. Alfrey, Jr. 1  
 Polymer Research Lab.  
 Dow Chemical Company  
 Midland, MI 48640

Prof. N. Brown 1  
 Metallurgy Dept.  
 Univ. of Pennsylvania  
 Philadelphia, PA 19104

Dr. S. Krimm  
Univ. of Michigan  
Ann Arbor, MI 48104

R. S. Marvin  
National Bureau of Standards  
Washington, DC 20234

1 Prof. John F. Fellers 1  
Polymer Science & Engineering  
Program  
419 Dougherty Engineering Building

1 University of Tennessee  
Knoxville, TN 37916